



---

**Forschungszentrum Karlsruhe**  
in der Helmholtz-Gemeinschaft

---

**Wissenschaftliche Berichte**  
FZKA 7120

# **Topology of Compressed Pebble Beds Determined by X-Ray Tomography**

**J. Reimann, R. A. Pieritz,  
M. di Michiel, C. Ferrero**

**Institut für Kern- und Energietechnik  
Programm Kernfusion**

**Juni 2005**



**Forschungszentrum Karlsruhe**

in der Helmholtz-Gemeinschaft

Wissenschaftliche Berichte

FZKA 7120

# **Topology of Compressed Pebble Beds Determined by X-Ray Tomography**

J. Reimann, R. A. Pieritz <sup>1)</sup>, M. di Michiel <sup>2)</sup>, C. Ferrero <sup>2)</sup>

Institut für Kern- und Energietechnik  
Programm Kernfusion

<sup>1)</sup> Applied Research Solutions, 444, Rua General Osorio, Blumenau, SC, Brazil

<sup>2)</sup> European Synchrotron Radiation Facility, B. P. 220,  
38043 Grenoble CEDEX, France

Forschungszentrum Karlsruhe GmbH, Karlsruhe

2005

**Impressum der Print-Ausgabe:**

**Als Manuskript gedruckt  
Für diesen Bericht behalten wir uns alle Rechte vor**

**Forschungszentrum Karlsruhe GmbH  
Postfach 3640, 76021 Karlsruhe**

**Mitglied der Hermann von Helmholtz-Gemeinschaft  
Deutscher Forschungszentren (HGF)**

**ISSN 0947-8620**

**urn:nbn:de:0005-071202**

## **Abstract**

In currently developed ceramic breeder blankets for future nuclear fusion reactors, both the ceramic breeder and beryllium are in form of pebbles. The thermal-mechanical behaviour of pebble beds strongly depends on the arrangement of the pebbles in the bed, their contacts with other pebbles and with walls and the related contact surfaces. The quantitative assessment of contact areas is of special importance for beryllium pebble beds because the thermal conductivity is ruled by this quantity.

Results from experiments are reported where, first, pebble beds consisting of 3.5mm aluminium spheres, (simulating the 1mm beryllium pebbles) were uniaxially compressed in the Forschungszentrum Karlsruhe at different pressure levels. Then, detailed three-dimensional microtomography experiments were performed at the European Synchrotron Radiation Facility in Grenoble. Three-dimensional views of the pebble arrangements and void fraction distributions were calculated. By further post-processing the data, the number of contacts between the particles, the corresponding contact areas and the angular dependence of these contacts were determined.

It has been shown that in uniaxial compression tests the poloidal distribution of contact surfaces is non-homogeneous. This fact should be considered when using these tests as standard tests for the generation of thermal-mechanical pebble bed data.

# **Bestimmung der Topologie von komprimierten Schüttbetten durch Röntgenstrahlen-Tomographie**

## **Zusammenfassung**

In derzeit entwickelten keramischen Brutblankets für Kernfusions-Reaktoren werden sowohl für das keramische Brutmaterial als auch für Beryllium granuläre Materialien (Pebbles) verwendet. Das thermomechanische Verhalten dieser Schüttbetten hängt wesentlich von der Anordnung der Pebbles im Schüttbett ab, ihren Kontakten mit anderen Pebbles und Wänden und den dazugehörigen Kontaktflächen. Die Kenntnis der Kontaktflächen ist von besonderer Bedeutung für Beryllium-Schüttbetten, da hier die thermische Wärmeleitfähigkeit sensitiv von den Kontaktflächen abhängt.

Es werden experimentelle Ergebnisse vorgestellt, wobei anstelle der 1mm Beryllium-Pebbles Schüttbetten bestehend aus 3,5mm Aluminium-Kugeln verwendet wurden. Die Schüttbetten wurden zunächst im Forschungszentrum Karlsruhe in uniaxialen Kompressionsversuchen mit unterschiedlichen Enddrücken komprimiert. Anschließend wurden in der European Synchrotron Radiation Facility, Grenoble, detaillierte dreidimensionale mikrotomographische Untersuchungen durchgeführt. Es wurden dreidimensionale Ansichten der Pebble-Anordnungen im Schüttbett sowie radiale und axiale Porositätsverteilungen berechnet. Durch weitere Datenverarbeitung wurden die Kontaktzahlen der Pebbles, die dazugehörigen Kontaktflächen und die Winkelabhängigkeit der Kontaktstellen bestimmt.

Es zeigte sich, dass in Uniaxialen Kompressions-Versuchen die poloidale Verteilung der Kontaktflächen nicht homogen ist. Diese Tatsache sollte bedacht werden bei der Verwendung dieser Versuche zur Gewinnung thermomechanischer Schüttbett-Daten.

**Contents**

- 1. INTRODUCTION ..... 1
- 2. EXPERIMENTAL ..... 3
  - 2.1. Uniaxial Compression Tests ..... 3
  - 2.2. Microtomography Set-up and Procedure ..... 5
- 3. MORPHOLOGICAL ANALYSIS ..... 8
  - 3.1. Results ..... 9
    - 3.2.3. Void fraction distributions ..... 16
- 4. TOPOLOGICAL ANALYSIS ..... 22
  - 4.1. Filtered Medial Line Skeleton ..... 22
    - 4.1.1. Filtered Medial Line Graph ..... 23
    - 4.1.2. Graph Node Classification ..... 23
  - 4.2. Data Model ..... 25
    - 4.2.1. Pebble Classes ..... 25
  - 4.3. Expected Results ..... 26
    - 4.3.1. Compression - Contact Surface Ratio - Coordination Number ..... 27
    - 4.3.2. Domain location and Edge Effects - Coordination Number ..... 27
    - 4.3.3. Class C2, C\_other and C\_noise - Coordination Number ..... 27
  - 4.4. Post-Processing ..... 28
  - 4.5. Topology Results ..... 29
    - 4.5.1. Post-processed Results ..... 29
    - 4.5.2. Sphere Positions ..... 32
    - 4.5.3. Contact Surfaces ..... 35
    - 4.5.3. Coordination Numbers ..... 38
    - 4.5.4. Poloidal Distribution of Contact Surfaces ..... 40
- 5. FUTURE EXPERIMENTS ..... 42
- 6. CONCLUSIONS ..... 43
- REFERENCES ..... 44
- ANNEX 1 ..... 46



## 1. INTRODUCTION

In the current design of ceramic breeder blankets for future fusion reactors, both the ceramic breeder and beryllium are foreseen to be in form of pebbles. During operation, thermal stresses cause pebble compression and with this pebble deformations. The description of the thermal-mechanical behaviour of these beds requires as input pebble bed data such as  $\text{strain} = f(\text{stress}, \text{temperature})$ ,  $\text{thermal creep} = f(\text{stress}, \text{temperature})$ ,  $\text{thermal conductivity} = f(\text{strain}, \text{temperature})$ , compare [1]. These data are currently obtained by performing uniaxial compression tests (UCTs) considering the pebble bed as a “black box”. Thus, investigations on the inner structure of the pebble beds including the arrangement of the pebble within the bed, the contacts of pebbles with the neighbouring pebbles or walls, and the corresponding contact zones can provide an important help in interpreting the results from thermal mechanical pebble bed tests.

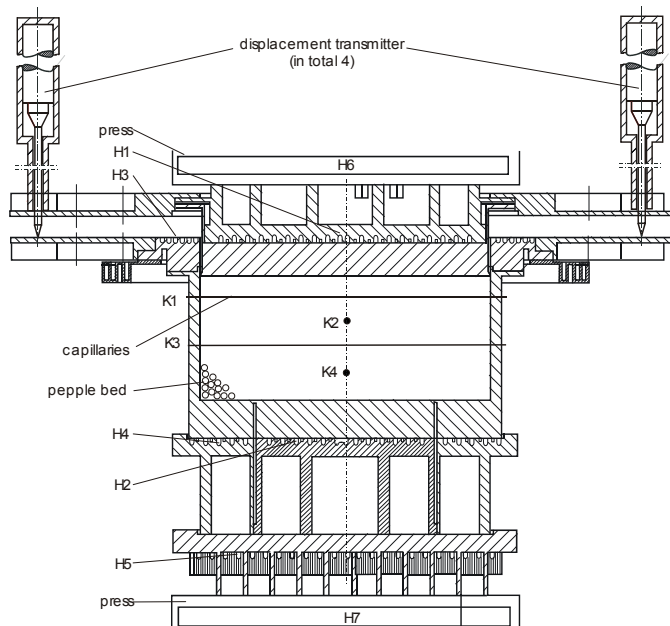


Fig. 1.1. HECOP-facility [2] for measurements of the thermal conductivity of beryllium pebble beds.

The assessment of contact areas is of special importance for granular materials with a large thermal conductivity compared to the surrounding gas conductivity (beryllium, aluminium) because in this case, the thermal conductivity depends sensitively on contact surfaces. Figure 1.1 shows an experimental set-up [2-3] where UCTs are combined with thermal conductivity measurements. A characteristic feature is that both the pressure and the heat flux are in the direction of the cylinder axis. Figure 1.2 contains characteristic results [1] for the relation between uniaxial stress and uniaxial strain for 1mm beryllium beds. The first stress increase period is governed by pebble relocation and elastic/plastic pebble deformation. Dur-

ing the stress decrease phase (steeper part of the curve) the pebble positions remain essentially unchanged and there is only a small effect due to elasticity. Figure 1.2 depicts also values of the thermal conductivity  $k$  : for a bed compression of about 1%,  $k$  increases by a factor larger than 5 compared to the non-compressed bed.

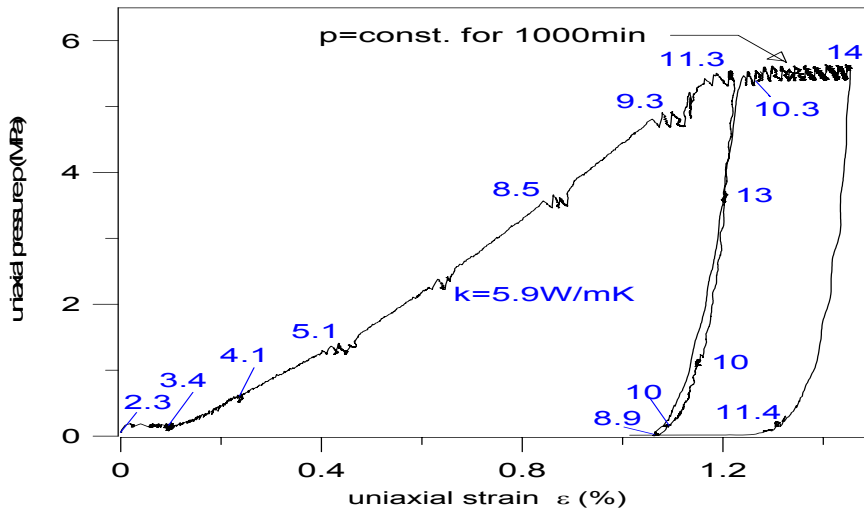


Fig. 1.2. Uniaxial compression test with beryllium pebble bed at 480°C [1].

Presently, for engineering applications, the Schlünder-Bauer-Zehner (SBZ) model [4] is often used to predict the thermal conductivity of pebble beds. In this model, the contact ratio  $A_c/A$  is an open parameter, where  $A_c$  is the contact surface and  $A$  the pebble cross section. Relationships which correlate the contact ratio  $A_c/A$  with the measured strain  $\epsilon$  are proposed in [2].

In order to improve heat transfer models to describe the thermal conductivity of pebble beds and the heat transfer coefficient between pebbles and walls, the knowledge of these contact surfaces and other topological quantities are required. Therefore,, a study by tomography of the 3D pebble bed structure, based on the use of synchrotron light, was performed in collaboration with the European Synchrotron Radiation Facility, a high intensity, high brilliance, 3<sup>rd</sup> generation synchrotron radiation source located in Grenoble, France. As a first step, pebble beds were compressed in the Forschungszentrum Karlsruhe to different stress levels in UCTs. For higher microtomography accuracy, the experiments were performed with aluminium spheres instead of the 1 mm beryllium pebbles used in the blanket. As a second step, in the European Synchrotron Radiation Facility (ESRF) Grenoble, computer aided micro-tomography (CMT) scans of the compressed pebble beds were performed, which allow reconstructing 3-D volumes of the attenuation coefficient of the X-ray beam within samples of different size, density and structural features, without physically damaging them. By post-processing the acquired data, useful quantitative information was obtained such as axial and radial void frac-

tion distribution in the samples as well as topologic parameters of the structure. First results of these investigations were presented recently [5].

In parallel to these investigations, similar experiments were performed with a compressed bed of 5mm aluminium spheres, where contact surfaces and coordination numbers were determined by optical microscopy. A comparison of first results from these experiments with microtomography results described in detail in this report were presented by [6].

## 2. EXPERIMENTAL

### 2.1. Uniaxial Compression Tests

The aluminium spheres had diameters of  $3.5 \pm 0.02$  mm. The spheres were filled in cylindrical aluminium containers (“cans”) with a height of 60mm, an inner diameter of 49mm and a wall thickness of 0.5mm. Filling was assisted by vibration; packing factors PF (ratio of solid volume to total volume) between 59.4 and 60.0 % were obtained, corresponding to void fractions  $\gamma$  (ratio of void volume to total volume) between 40.6 and 40%. For the UCTs, the filled cans were placed inside of a thick-walled cylindrical steel container, see Fig. 2.1.

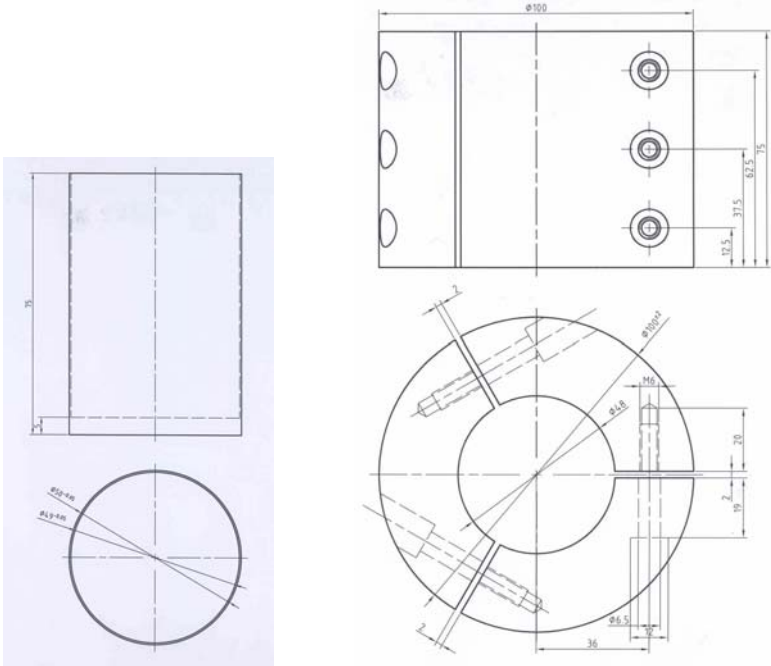


Fig. 2.1. Aluminium can and steel container for present experiments

Figure 2.2 shows the uniaxial stress-strain curves of the experiments performed up to maximum pressures of 16 MPa and strains up to 10%. During stress decrease, strain changes only marginally, indicating that elastic stresses are negligible compared to plastic

pebble deformations. This is an important point because the goal was to perform the microtomographic investigations with pebble beds representative for the compressed state. In order to achieve this, the cans were closed under maximum piston pressures in such a way that after releasing the piston pressure a small residual pressure remained. For the

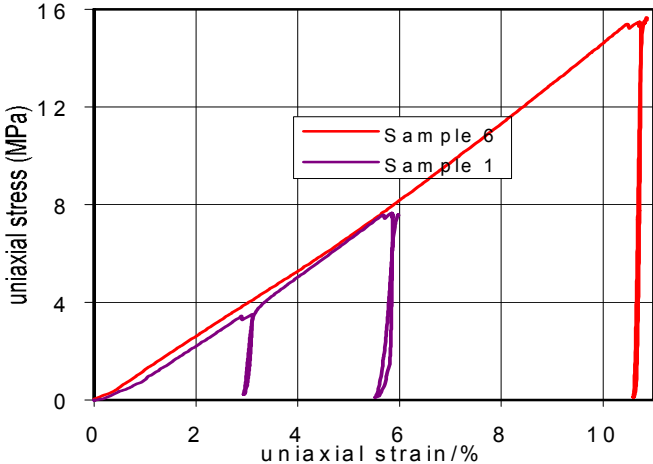


Fig. 2.2 Uniaxial compression tests with pebble beds consisting of 3.5 aluminium spheres.

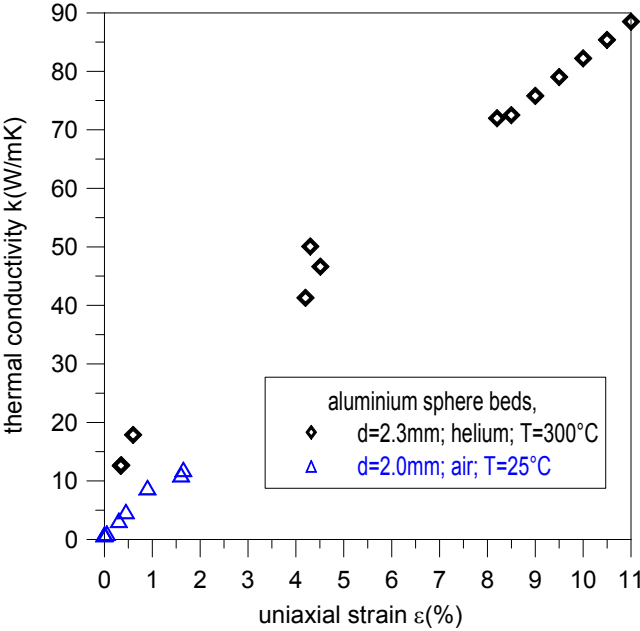


Fig. 2.3 Thermal conductivity as a function of strain for aluminium pebble bed (2mm diameter aluminium spheres).

microtomography, besides samples S1 and S6, a sample without pre-compression (S0) was also used.

From previous measurements, a few thermal conductivity data exist for pebble beds consisting of 2mm aluminium spheres, performed in air at ambient temperature. Recently new measurements were performed with 2.3mm aluminium spheres in helium at  $T=300^{\circ}\text{C}$  with a maximum strain of  $\approx 11\%$ , see Fig. 2.3. Again, the strong increase of thermal conductivity with increasing compression is evident.

## 2.2. Microtomography Set-up and Procedure

In this section, the 3-D x-ray micro-tomography system which was used for the experiments and which had been developed at the High Energy Beamline ID15A of the ESRF is presented. The ID15 set-up has the ability of acquiring volume image data at a very high speed. This speed has been made possible by combining a high efficiency CCD detector technology with a very intense high-energy white beam radiation. The useful x-ray energy spectrum for tomography applications spans from 40 keV to 250 keV and is consequently very suitable for high Z materials or for sizeable samples, which highly absorb the incident radiation. The x-ray spectrum can be modified by inserting different filters into the x-ray beam in order to optimise the signal-to-noise ratio (SNR) and avoid beam hardening. The main set-up parameters are briefly described hereafter.

The experimental set-up is schematically illustrated in Figure 2.4. It consists of a high precision stage to position the sample in the x-ray beam and an imaging detector system. The sample positioning system has double tilt stages and a translation stage for the alignment of the rotation axis with respect to the detector, as well as micro-positioning x-y-z stages for sample alignment. The x-rays are converted to visible light via a phosphor screen. Light is collected and focused by a set of optical lenses to the DALSTAR camera, compare [7]. The whole equipment is mounted on a marble table to reduce vibrations.

Two configurations for the imaging systems are available: “low resolution” and “high resolution”. The low-resolution (higher than or equal to  $14\ \mu\text{m}$ ) configuration is customarily used for samples with a diameter greater than 10 mm and the high-resolution one (down to  $2\ \mu\text{m}$ ) is recommended for sample diameters comprised between 1 and 10 mm. The low-resolution set-up was used for our experiment and is shown in Fig. 2.5. A Cerium doped YAG scintillating crystal is used. The visible light emitted by the YAG:Ce scintillator is focused by a macro-objective onto the CCD camera, see [8]. Thanks to the long working dis-

tance of the objective a 45° mirror can be placed between the scintillator and the optics in order to protect the lenses and the detector from the direct high-energy x-ray radiation.

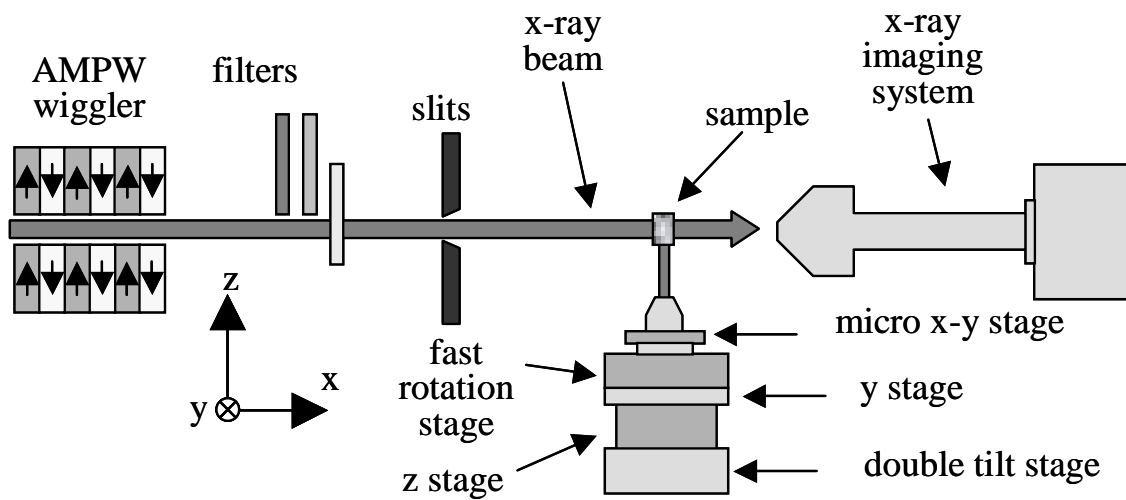


Fig. 2.4 G 4. Schematic view of the x-ray micro-tomography experimental set-up at the ESRF ID15A beam-line. The radiation source is a 7-pole asymmetric wiggler. The x-ray white spectrum is adapted to the different samples by changing the wiggler magnetic field as well as by means of filters.

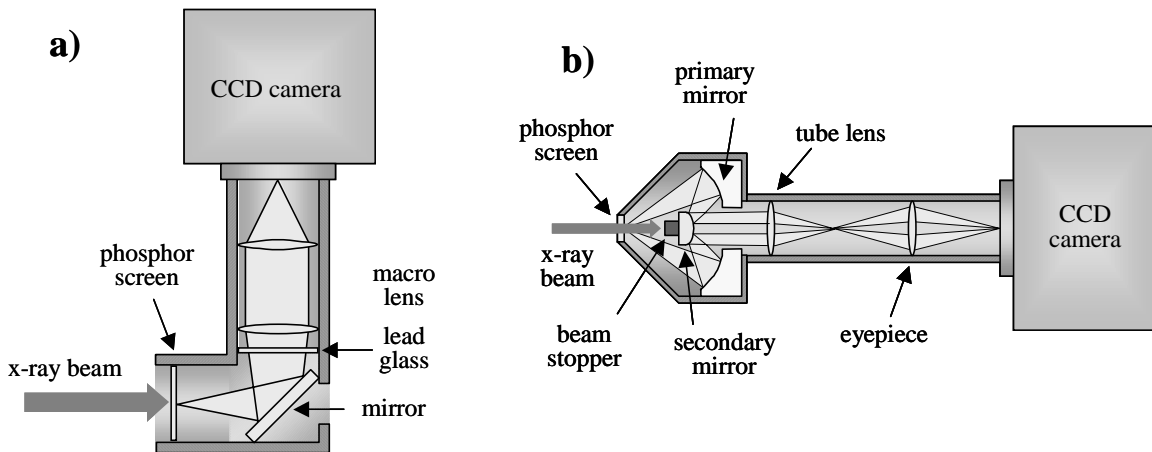


Fig. 2.5 (a) “Low resolution” and (b) “high resolution” imaging detector.

The CCD consists of 1024x2048 pixels of  $14 \times 14 \mu\text{m}^2$  size each. In frame transfer mode half the area of the chip (1024x1024 pixels) is reserved for charge storage and the other half for photon detection. After exposure the image is transferred in 0.84 ms to the storage region for read out and the data acquisition is started again. A considerable benefit of this architecture is that no mechanical shutter for the x-ray beam is required.

The readout speed can be increased from 60 to 110 frames per second when operating in 2×2 binning mode. The data transfer from the camera to the computer memory is done using two frame grabber boards. Due to the high data rate the images are temporarily stored in the computer memory and only at the end of each tomographic scan they are saved onto disks, for details, see [9-10]. The nominal write speed is 120 MB/s.

After every scan, a tomographic reconstruction of a single slice can be performed on a data processing computer in order to monitor the correctness of the acquisition or, if applicable, the evolution of the sample.

The tomographic reconstruction is performed using a filtered back projection algorithm. Since every sinogram is treated independently the computation has been parallelized. The typical reconstruction time for a volume of 1024×1024×1024 pixels is one hour.

In our case a resolution of 28 μm was chosen (2x2 binning mode). About 1800 projections were recorded for every sample sub-volume at an angular rotation pace of ~0.1 deg. Each scanned sub-volume (elementary volume) was about 2 mm high and 30 mm wide, corresponding to the beam size at the sample location. Two of such elementary volumes juxtaposed in the horizontal direction were needed in order to cover the entire sample diameter. Vertical stacks of elementary volumes (right and left) were swept by the beam in order to explore sample regions of at least 7-8 mm height. The total scan time per stack was about 8 hours and it took 2 days for pre-processing and reconstructing each stack. Globally some 300 GByte data had to be processed.

### 3. MORPHOLOGICAL ANALYSIS

**Main concepts and methods:** Assessment of the void fraction distribution within a packed bed is essential for rigorous heat flow analysis and mechanical evaluation. The main morphological parameter used to characterise the heat and mass flow through a pebble bed is the surface and the volume ratio (or the void fraction) of the individual elements or the statistical data of the entire bed. The second parameter analysed is the influence of the wall on the arrangement of the pebbles in the bed, described by the axial and radial void distributions. The rationale of the morphologic analysis as described by [11] has been applied to exploring the surface and volume ratios of the sampled can data. The analysis of the sample set allows observing the influence of the compression ratio on the volume and surface ratios.

**Surface and Volume:** The common approach to evaluate the volume and surface shapes in a discrete domain (computer aided analyses) is based on a voxel counting to evaluate volumes and surfel counting to evaluate surfaces (a cubic voxel has six surfels i.e. six sides). This method is extremely rapid but the associated errors can be enormous: >40% for the surface evaluation and >10% for the volume evaluation (depending on the object shape complexity). Other methods using Euclidean metrics based on triangles extraction over isometric surfaces like “marching cubes”, “level set” (72 times bigger in volume data size) or discrete surface normal/projection techniques [12] [13] are processor and memory consuming. These methods cannot be used over extremely large data sets (as in the present case).

To bypass this limitation we use a volume-surface and voxel integration method [14], based on the analysis of the voxel neighbourhood. The method consists to labelling the surface voxel by analysing its 26 surface neighbours. A label is attributed indicating the surface and the volume average as a function of the topology of the surrounding surface elements. The associated volume and surface measure error can by that be reduced to less of 2% [14] for large voxel size objects (10 voxel radius or more). The related algorithm runs only once over the data matrix in order to label and measure objects, allowing high speed and low memory consuming.

The main pebble radii are analysed using a 3D discrete distance map [15] [16], representing the maximum spheres inscribed in the non-void volume shape. This approach needs to run through the data matrix only twice, using just integer labels. The associated max error using a 3D large mask kernel (45 elements) is less than 0.5% in length.

The main computational measurements illustrated here show the pebble bed surface and the volumes of the solid and void fractions related to the selected ROI (in this case a cylinder).

**Axial and Radial Void Fraction:** The method to analyse the wall perturbation induced in the pebble network arrangement (pebble connections) is similar to that reported by [17-20] The common voxel counting approach is followed, where the relative error has no influence over the data analysis.

The axial void distribution is obtained by counting the void fraction for each slice in the Z (vertical) direction. One subdivides numerically the cylindrical can in concentric sub-cylinders, each of 1 voxel thickness. From the external wall down to the central axis one counts up the void fraction of each sub-cylinder thickness. The results show the variation of the axial void fraction due the external wall can. This parameter shows the oscillation of the void fraction due the external radial wall can. Analysing these results we can observe the structural influence of the axial compress ratio in the pebble arrangement (all samples).

### 3.1. Results

#### 3.2.1. General comments

It should be recalled at this point that the data were acquired by small sub-domains of the whole cans (10 sub-domains, each of 20 mm height and 30 mm width, corresponding to the beam window size) owing to the required resolution (28  $\mu\text{m}$ ). The sample core portions to be analysed were assembled going through the following work steps:

- i) byte order inversion (due to using computer platforms with opposite byte ordering for the data acquisition and for the data analysis);
- ii) byte size re-scaling (from floating point numbers to one byte integers);
- iii) grey level scaling;
- iv) cutting of sub-domains (wherever slight overlapping occurred of juxtaposed sub-domains);
- v) rotation axis alignment (also due to sub-domain imperfect juxtapositions) ;
- vi) Region of Interest (ROI) definition;
- vii) threshold setting in order to obtain the final geometric volume (at this step one discriminates between matter and void (or, equivalently, air), by labelling each of them with only one colour, either white or black). The regions outside the ROI will be marked with grey colour;
- viii) cutting out non-ROI domains (like can walls, etc).

In the following, the main results are shown for the four scanned sample portions scanned in the three different cans. The positions of the sample core portions in each of the cans was shown in Section 2.2. In Table 3.1, the geometric quantities of all scanned sample portions are summarised.

For each sample portion, the following quantities are presented:

- the horizontal cross section at  $Z=0$  of the ROI sample (solid pebbles in white, void fraction in black and non-ROI domain in grey),
- the vertical cross section through the central axis of the ROI, and
- a 3D rendering view of the reconstructed volume;
- two graphs, one displaying the axial and the other the void fraction profile, the first as a function of the co-ordinate  $Z$  along the cylinder axis and the second as a function of the radial distance  $d$  from the ROI lateral surface. The origin of  $Z$  is fixed at the top surface of the cylindrical irradiated ROI, whilst the origin of  $d$  is located at the inner wall of the can.

It should be noted that:

- the cylindrical ROI volume is smaller than the total data volume since some parts of the latter, like the can walls were cut out while defining a perfectly cylindrical ROI. One ought to bear in mind that, strictly speaking, the can horizontal cross section is not exactly circular, at least in the mathematical sense
- also the pebbles are not mathematically spherical, thus the pebble main diameter is defined as the diameter of the largest perfect sphere inscribed in the pebble
- the void and the solid fraction, the total and the specific surface of the solid fraction refer to the ROI volume;
- the max length measurement error is about  $\pm 2\%$ ;
- the experimental and therefore numerical resolution is about  $\pm 1$  voxel ( $28 \times 10^{-6}$  [m]).

### **Pebble visualisation**

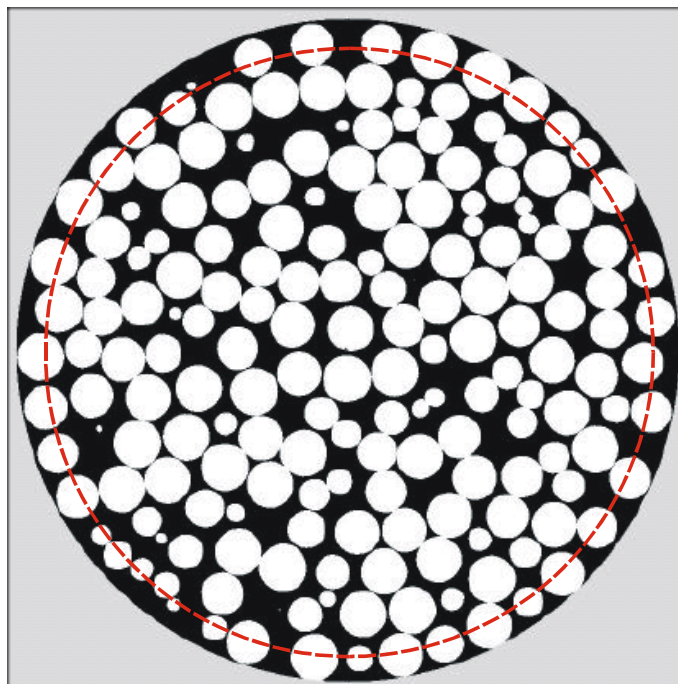
Table 3.1 summarises the main data on the morphological quantities; the following Figs. 3.1 – 3.12 contain details for the individual samples.

Table 3.1. Main results morphological quantities.

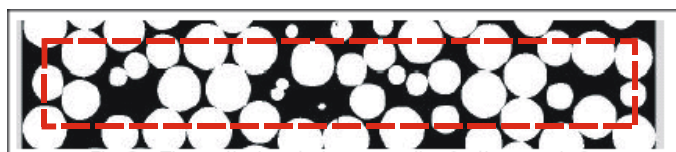
<b>Sample</b>	<b>S0</b>	<b>S1</b>	<b>S6mid</b>	<b>S6bot</b>
Compression (MPa)	0	8	16	16
Total data volume (cm <sup>3</sup> )	23.17	18.90	16.39	20.45
Cylindrical ROI volume (cm <sup>3</sup> )	17.42	14.24	12.30	15.37
ROI diameter (cm)	4.83	4.83	4.83	4.83
ROI height (mm)	9.52	7.78	4.83	4.832
Void fraction (%)	38.76	37.41	34.65	37.01
Solid fraction (%)	61.24	62.52	65.35	62.99
Total solid fraction surface (without ROI edges) (cm <sup>2</sup> )	164.3	131.8	113.09	140.35
Specific surface of solid fraction (in the volume excluding the ROI edges) (1/m)	945.4	927.63	921.75	915.10
Mean pebble diameter (mm)	3.427	3.427	3.427	3.427

From Figs. 3.1-3.4 it might be concluded that the arrangement of spheres is quite irregular except close to the cylindrical wall where most of the spheres are in contact with the wall. Because the can cross section was not ideally circular, the selected ROI diameter had to be smaller (48.3 mm) than the average inner can diameter of 49 mm, with the consequence that the outer sphere volumes were often cut, see figures c). Therefore, this flattening of the outer sphere surface must not to be mixed with flattening caused by mechanical deformation. Figure 3.1a) and b) contains (in red) boundaries which mark the inner volume which is used for the topological analyses outlined in Section 4.

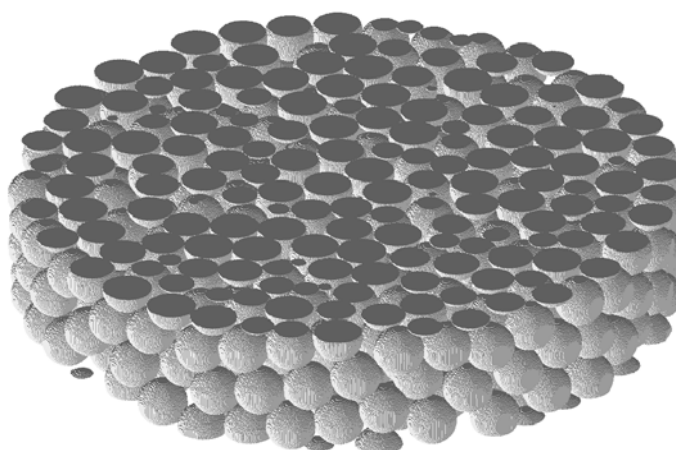
The different degrees of compaction and different contact surfaces are difficult to observe in the figures. However, interesting details can be detected concerning the sphere structures at the bottom of the core samples. As already mentioned, the exact vertical position of the ROIs was not known but it was known that the core sample S1 was closest to the can bottom. Fig. 3.2b) shows that nearly all sphere centres close to the ROI bottom are on the same height indicating that this layer of spheres is probably in contact with the bottom (1st layer). The same is true for S6bot although in this case the ROI has a slightly larger distance to the can bottom. This sphere positions close to the bottom and the cylindrical walls will be analysed in more detail in Section 4.5.3.



a) horizontal cross section, (1762 x 1762 x 340 voxel)

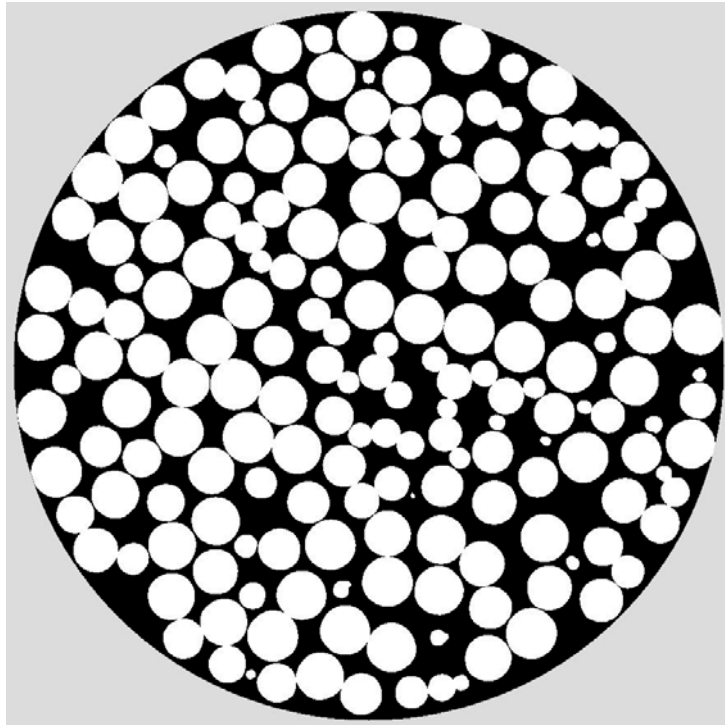


b) vertical cross section



c) 3D rendering of the scanned volume

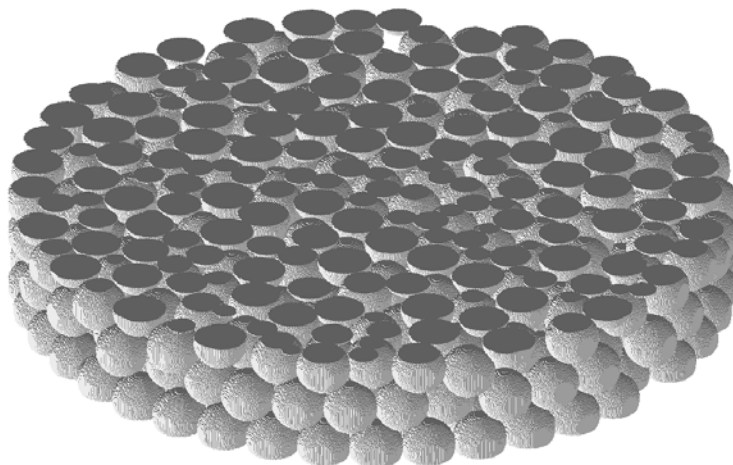
Fig. 3.1. Morphology of sample S0.



a) horizontal cross section, (1760 x 1760 x 260 voxel)

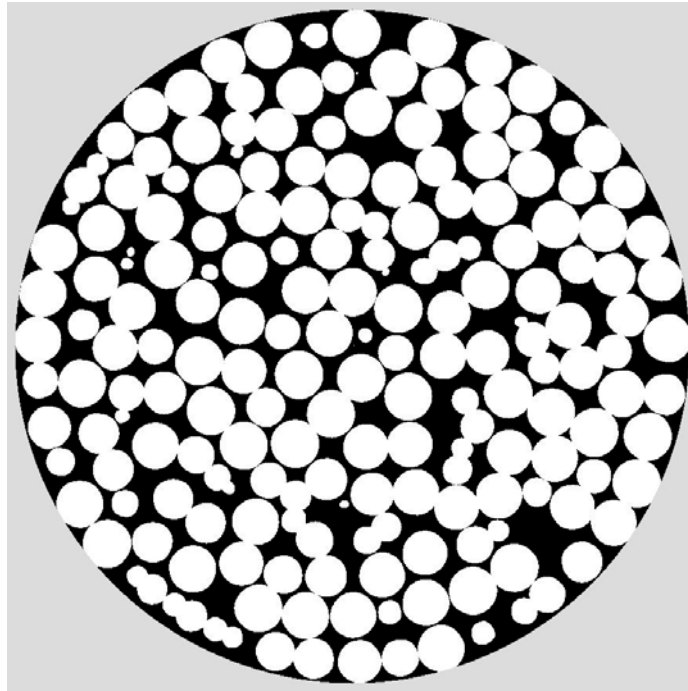


b) vertical cross section



c) 3D rendering of the scanned volume

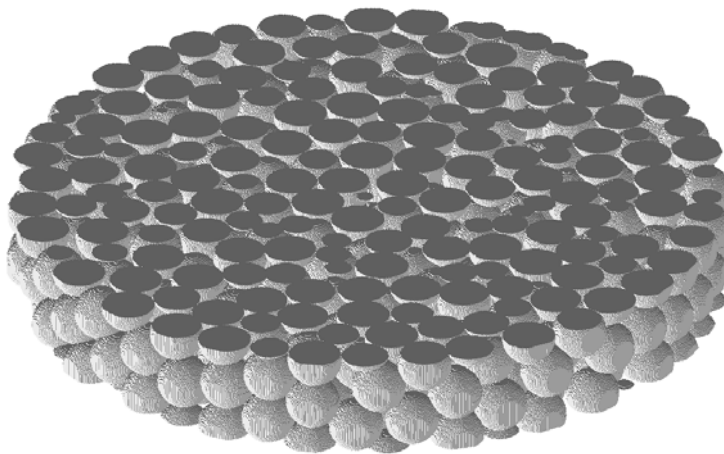
Fig. 3.2. Morphology of sample S1.



a) horizontal cross section, (1764 x 1764 x 240 voxel)

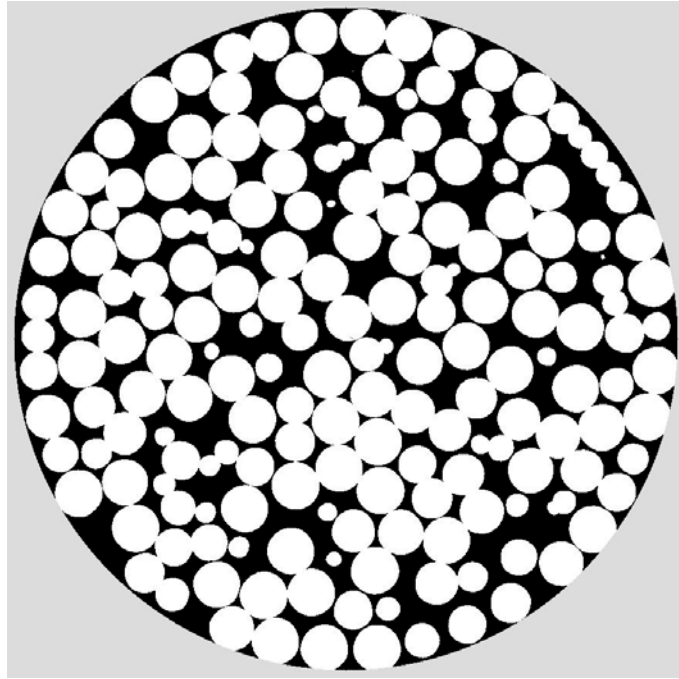


b) vertical cross section

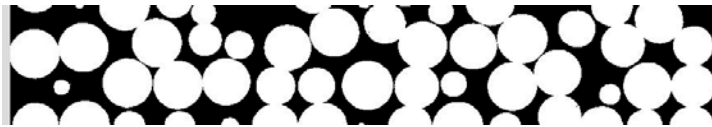


c) 3D rendering of the scanned volume

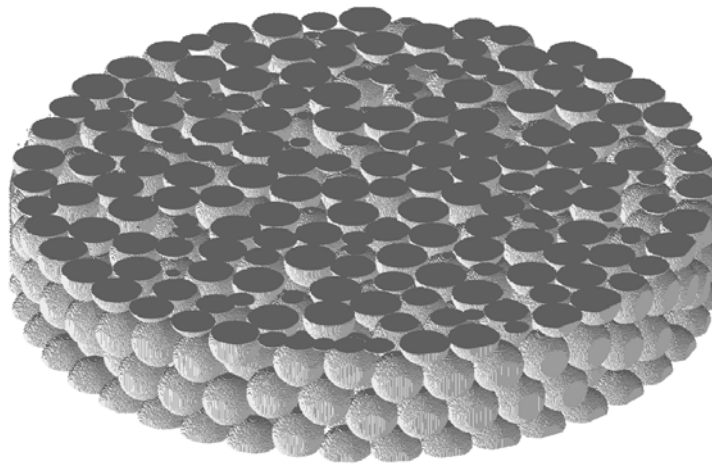
Fig. 3.3. Morphology of sample S6mid.



a) horizontal cross section, (1762 x 1762 x 300 voxel)



b) vertical cross section



c) 3D rendering of the scanned volume

Fig. 3.4. Morphology of sample S6bot.

### 3.2.3. Void fraction distributions

For fusion reactor blanket design, the knowledge of void fraction distribution within packed beds is essential for analyses of heat transfer characteristics within the bed and close to surrounding walls. In chemical engineering, packed beds are used for mass transfer processes. Non-homogeneous void distribution results in non-homogeneous flow distribution and with this non-homogeneous mass transfer [21,22].

Void fraction variations close to circular or plane walls are caused by the fact that during filling, the outermost spheres are generally in contact with the walls, arranged in a pattern which is close to the hexagonal pattern. For non-compressed beds, the void fraction must be unity at the wall since these spheres have only point contacts. Proceeding from the wall, the voidage must decrease and reaches a minimum at the wall distance of about 1 sphere radius, depending on the ratio of container diameter  $D$  to sphere diameter  $d$ , compare [18]. For the perfect hexagonal pattern the void fraction is at this distance  $\approx 18\%$ , in practice, values slightly above 20% are observed. With increasing distance, the void fraction increases, however, not to 100% since the second row of spheres rests in the cusps formed by the spheres in the first row. Proceeding in from the wall, the pattern is repeated and, since each row is more random than the row which precedes it, the amplitudes of the oscillation decrease and are damped out after a distance of 4-5 sphere diameters.

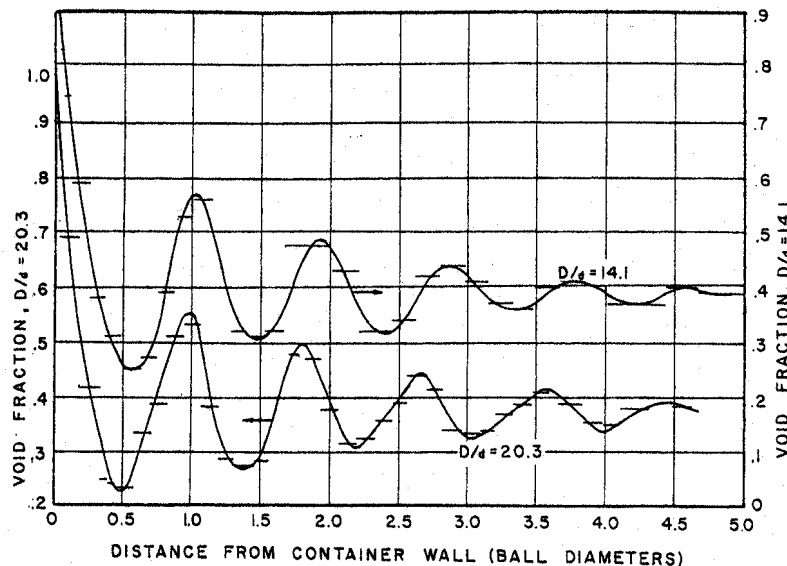


Fig. 3.5. Radial void fraction distribution [18]

Void fraction variations close to circular or plane walls were measured first more than 4 decades ago using time consuming destructive techniques [18]. Figure 3.5 contains characteristic results for non-compressed pebble beds and shows the radial distributions in cylindrical containers for two different ratios of container diameter  $D$  to sphere diameter  $d$ . First results on void fraction distribution obtained by microtomography were presented by [23], again using non-compressed pebble beds.

A correlation to describe these void fraction fluctuations was first proposed by [20] and later modified by others [21,22]. In the following, the correlation used by [21] is applied expressing the void fraction as a function of the normalised distance from the wall  $z = y/(d/2)-1$ :

$$\begin{aligned} \text{for } z < 0: \epsilon_{\text{wall}} &= \epsilon_{\text{min}} + (1-\epsilon_{\text{min}})z^2 & (3.1) \\ \text{for } z > 0: \epsilon_{\text{core}} &= \epsilon_0 + (\epsilon_{\text{min}} - \epsilon_0) \exp(-z/c)\cos(\pi z/b), \end{aligned}$$

where  $\epsilon_{\text{min}}$  is the minimum value at  $z=0$  and  $\epsilon_0$  is the value far away from the wall. The following values were used:  $\epsilon_{\text{min}} = 23\%$ ;  $\epsilon_0 = 39\%$ , and  $c = 4$ .

For  $D/d=\infty$ ,  $b$  has the value for ideal hexagonal packing,  $b=0.816$ , see below. Otherwise, a value of  $b=0.876$  is recommended which was found by [18] for  $D/d=20.3$ .

In the present case,  $\epsilon_{\text{min}}$ ,  $\epsilon_0$ , are taken from the experiments, and  $c$ , and  $b$  are considered as parameters.

Figures 3.6b-3.9b show the radial void fraction distributions; all results are presented in Fig. 3.10a). For compressed beds, the void fraction at the cylindrical wall is expected to be smaller than 100%. The distance between the void fraction minima is  $d \cos(35^\circ) \approx 0.82 d = 2.87\text{mm}$  for non-compressed beds with an ideal hexagonal dense packing (face centred cubic array). The curves for S1 and S6bot are influenced by the fact that the pebbles are also close to the bottom plate.

Figure 3.10 b) shows only the results for the samples S0 and S6mid: the data are fitted best using  $c=5$  and the values for  $b$  shown in the figure. There is the tendency that with increasing compression the curves should shift to lower void fractions and the distance between the pebble rows becomes smaller.

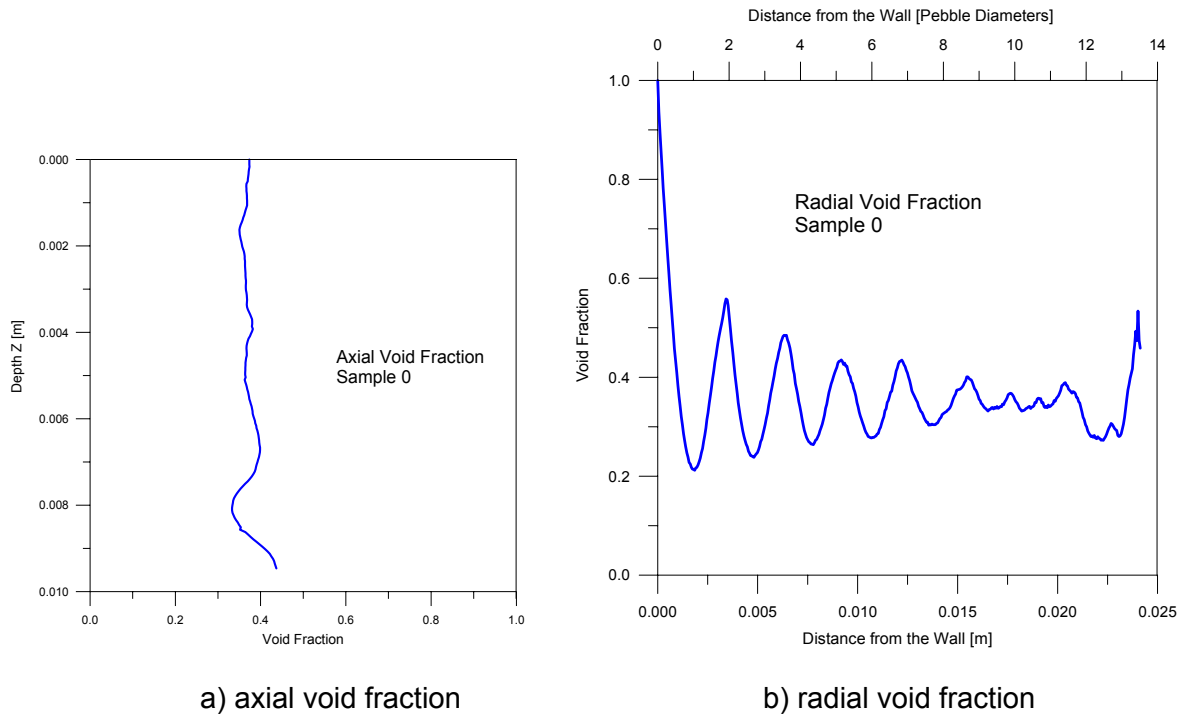


Fig. 3.6. Void fraction profiles for sample S0.

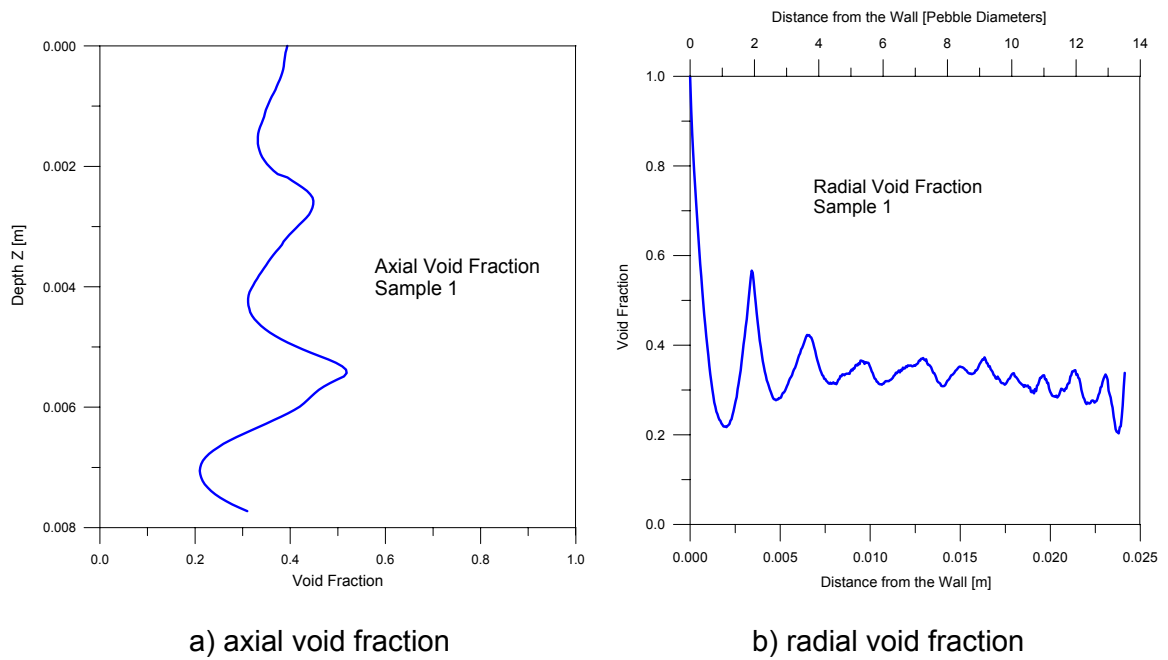
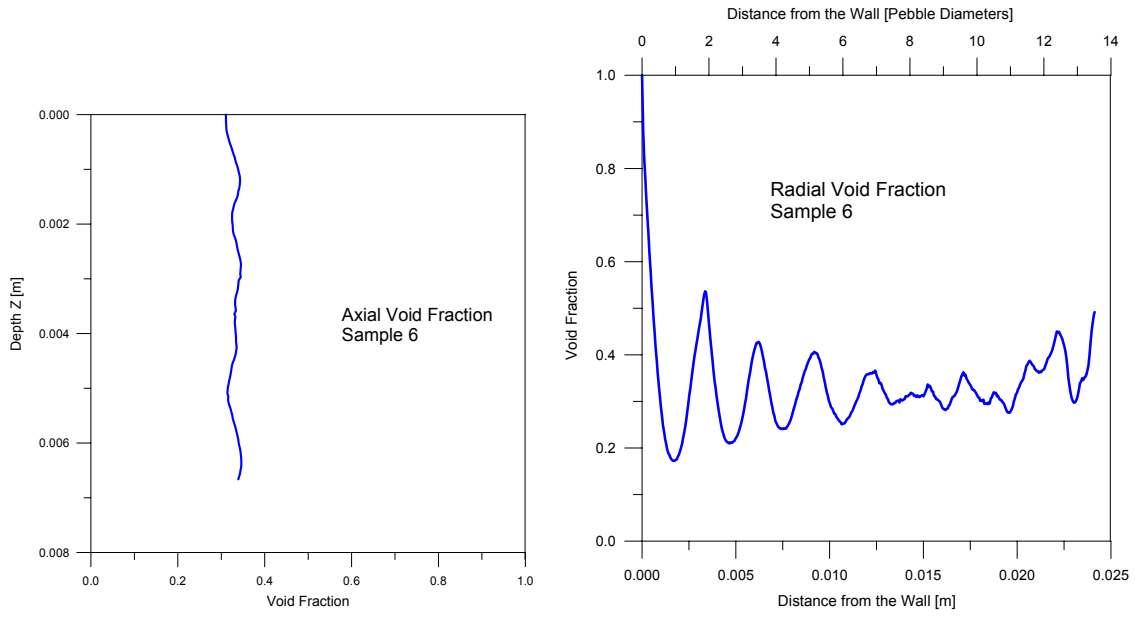


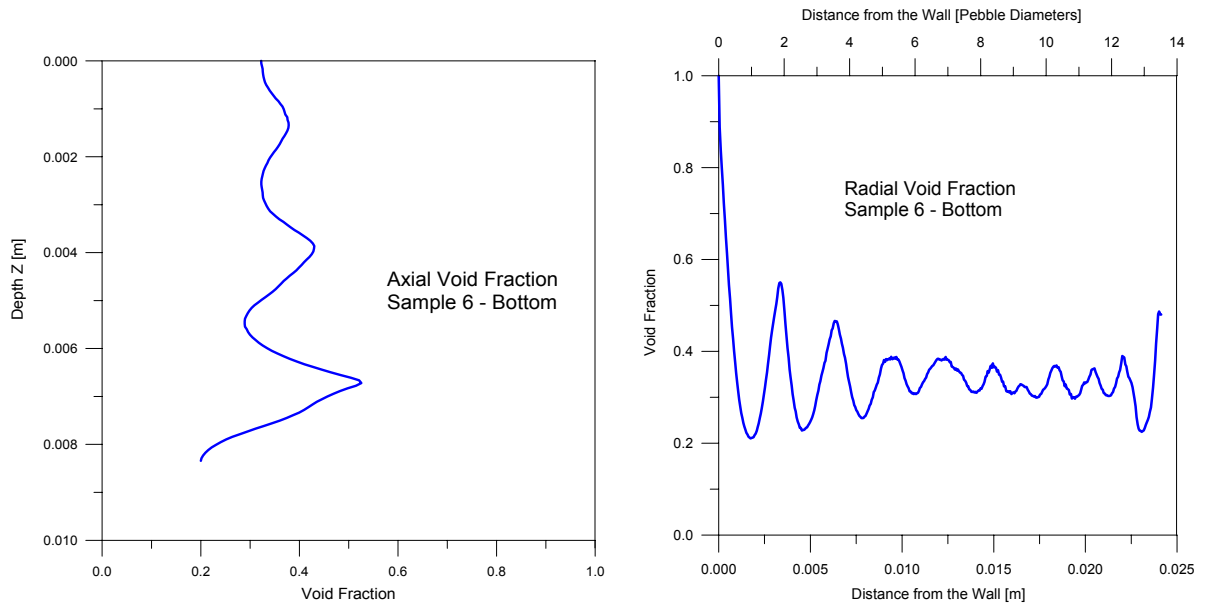
Fig. 3.7. Void fraction profiles for sample S1.



a) axial void fraction

b) radial void fraction

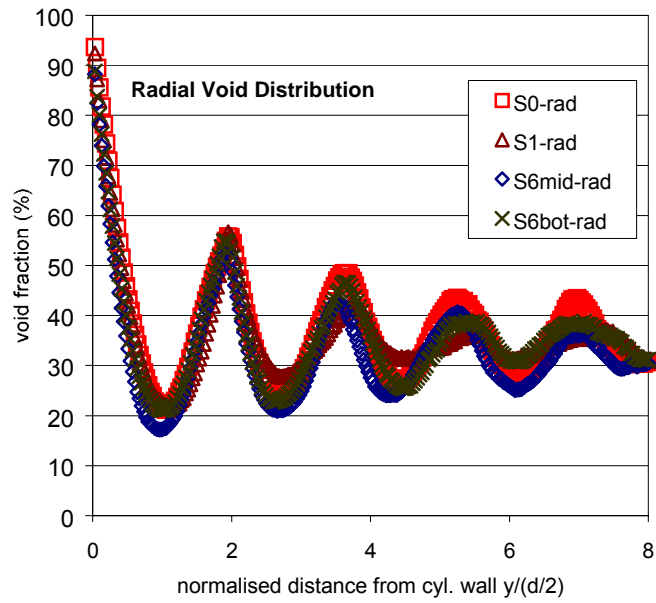
Fig. 3.8. Void fraction profiles for sample S6mid.



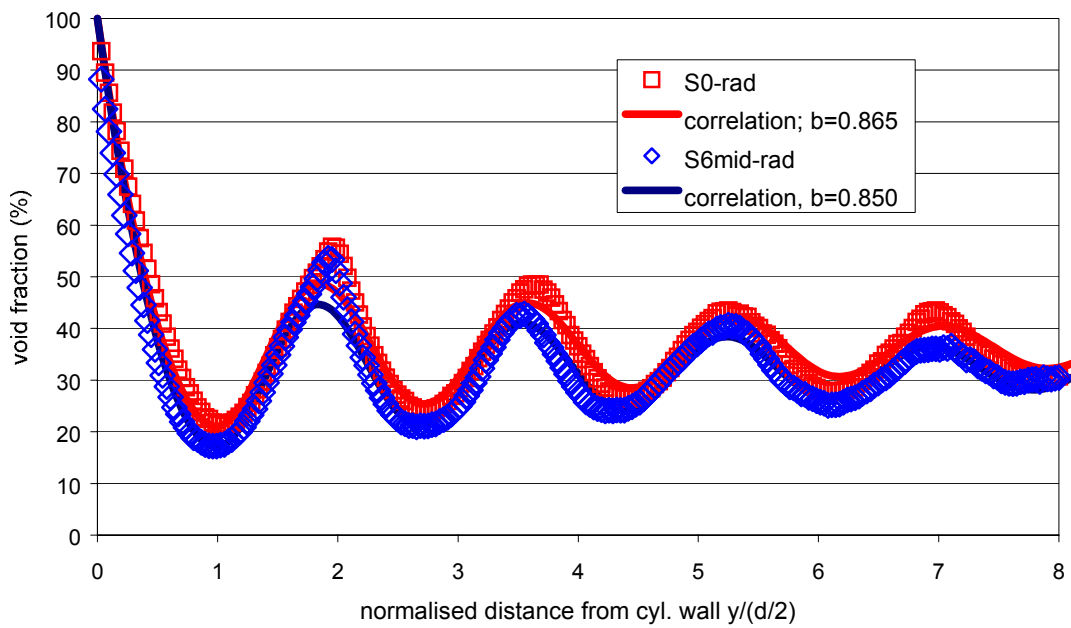
a) axial void fraction

b) radial void fraction

Fig. 3.9. Void fraction profiles for sample S6bot.

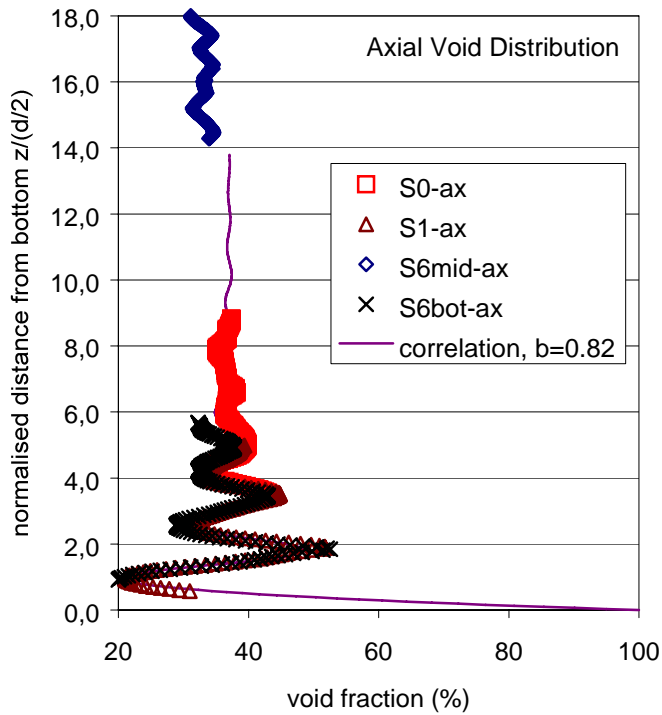


a) all data

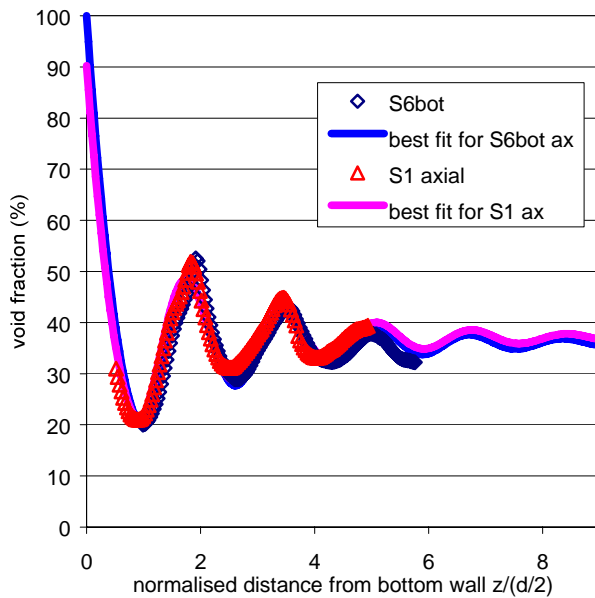


b) details for samples S0 and S6mid

Fig. 3.10. Radial void fraction distributions.



a) all data



b) details for samples S1 and S6bot

Fig. 3.12. Axial void fraction profiles.

In respect to the absolute void fraction values, the present measurements might not give the correct values because the ROIs heights are not sufficiently large compared to the sphere diameter of 3.5mm in order to give relevant volume averaged values.

Concerning the axial void fraction profiles, the exact position of the core sample bottom is, as mentioned, not known. If it is assumed that the lowest minimum for S1 belongs to the 1<sup>st</sup> layer of spheres, then, this layer is also partly seen in S6bot. Comparing all curves, it is then concluded that the minimum for S0 belongs to the 3<sup>rd</sup> layer; for larger distances from the bottom the void fraction becomes quite uniform, similar to the expected behaviour for S6mid. Figure 3.11 a) summarises all results; Fig. 3.11 b) shows the first cycles in more detail. The measured results are well fitted by Correlation (3.1) using a value of  $b = 0.82$ . For compressed pebble beds, the void fraction at the wall should not reach the value 1. In future experiments, this zone will be considered with special attention.

## 4. TOPOLOGICAL ANALYSIS

The primary goal of this analysis is to determine the main pebble radius, the position of the pebble centres in Cartesian co-ordinates, the contact areas and the coordination number of the individual pebbles. The coordination number is the number of connections for each element in the volume. The methodology employed here is based on a topologic operator called filtered medial line (FML) applied on the whole data volume (ML skeleton) and the corresponding graph representation (FML graph), as proposed by [16].

### 4.1. Filtered Medial Line Skeleton

The starting point of this method is the data volume in binary format (black and white representation), which is used to generate a discrete distance map. This map represents the largest spheres inscribed in the individual objects of the total volume. The first step in order to classify these spheres consists in identifying the connections of the different objects and in building a completely connected skeleton called medial line. A segment of the skeleton which has a width (diameter) of 1 voxel is called line.

The approach commonly followed in 3D analyses for identifying the ML skeleton would generate an extremely complex surface (not a line), preventing the recognition of simple structures over this “hyperconnected” shape. To bypass this limitation a filter is applied conserving the initial Euler number  $e_0$  of each connected object in the ML. The resulting topologic variety is called filtered medial line (FML). For each connected object  $C_n$  of the volume  $Y$  (entire domain), we verify whether a voxel  $P$  belongs to the filtered skeleton by checking if it satisfies the relation (1):

$$e_0(C_n \{P_0, \dots, P_i, \dots, P_n\}) \neq e_{n-i}(C_{n-i} \{P_0, \dots, P_n\}) \Rightarrow P_i \subset C_n \text{ and } P_i \not\subset C_{n-i} \text{ with } C_n \in Y \quad (1).$$

#### 4.1.1. Filtered Medial Line Graph

The FML Graph representation is based on the detection of the main elements and linking segments in the voxel structure arrangement of the FML. The classification of this objects set gives a complete topologic description of the volume.

The graph representation of the FML is only an abstraction where connection segments (denominated arcs) between main elements (denominated nodes) are identified. Nodes represent the centres of the largest spheres inscribed in the elementary volumes and are found by inspecting the 26 neighbouring voxels over the ML. When two nodes are found to be adjacent pixels they are considered to constitute the same node. Adding the 26 voxel neighbours taken over the median line gives the complete node characterisation. This addition is necessary to prevent the formation of redundant arcs. The remaining voxels on the ML generate arcs which connect the different nodes already found. The above procedure has been tested in several situations and proven to be suitable for the description of 3D images with a large distribution of very fine objects, with constrictions or protuberances of 3 to 4 voxel size: this situation is very frequent in porous structures studies.

#### 4.1.2. Graph Node Classification

Each element (voxel) of the ML is coded either as a node or as an arc, and then each node can be associated to the arcs starting from it and classified following the kind of connections generated. Four kinds of nodes can be identified, useful in structure identification:

- i) main nodes, which do not have connections with larger nodes;
- ii) large nodes, which have one connection with at least another large node and the others with smaller nodes ;
- iii) strict nodes, which have only one arc connected to a larger node;
- iv) connection nodes, which connect two or more larger nodes.

For our purposes we needed to explore only the main and the connection nodes.

In Fig. 4.1.a-b is shown a six spheres arrangement: four spheres the centres of which lie in the same plane, 1 sphere above this plane and 1 below (not centred on the axis passing through the geometric mid point of the centres of the four spheres and orthogonal to their plane). All spheres have the same radius value: 11 voxel. The ML skeleton is shown in figure 4.1.c by its voxel representation. The corresponding ML graph is shown in Fig. 4.1.d, where red balls represent the main nodes; green balls represent the connection nodes; and blue lines and balls represent the arc elements. For this example, we have six spheres each connected to four nodes (mean coordination number = 4).

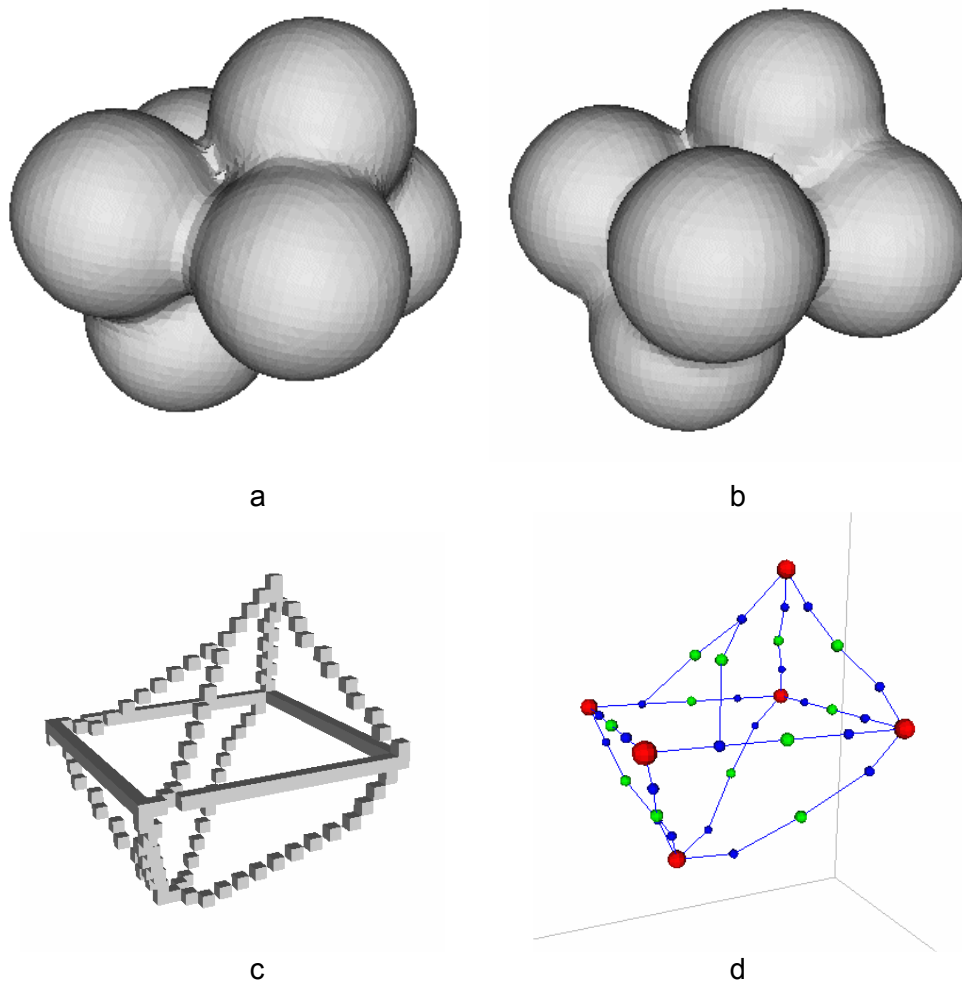


Fig. 4.1. The different steps in the FML Graph extraction: a, b) a six spheres arrangement c) ML skeleton (voxel view) and d) ML graph representation (main nodes in red, connection nodes in green, arcs in blue).

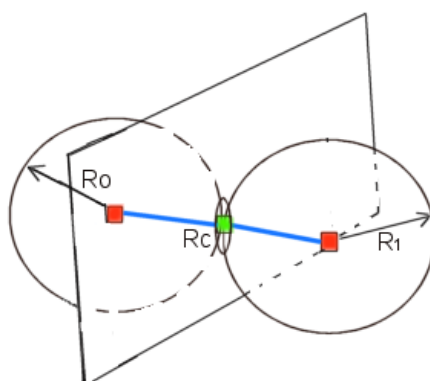


Fig. 4.2. Sphere representation of main nodes with centres  $R_0$  and  $R_1$  (in red) and connection plane shape with centre  $R_c$  (in green) (circular area in the plane).

## 4.2. Data Model

The main nodes and the connection nodes represent object centres by their coordinates (i, j, k). The main node radius represents an ideal sphere and the connection node radius represents an ideal circular shape (not a volume but just only a surface).

### 4.2.1. Pebble Classes

Different classes of pebbles, or better spheres (Fig. 4.3) can be identified in the samples due the existence of partial can domains (irradiated can regions) resulting from the geometry of the experimental data acquisition [24].

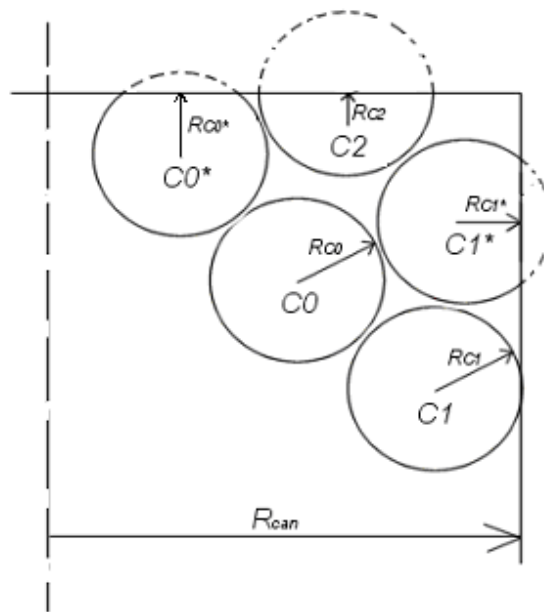


Fig. 4.3. The different classes of pebbles inside a partial domain, representing different radii and coordination numbers.

The main classes are:

- 1 – **class C0**: spheres entirely inside the domain (main coordination number, and radius  $R_{C0}$ );
- 2 – **class C0\***: spheres partially inside the domain (touching the top or the bottom of the can, coordination number is less than in class C0, and  $R_{C0} > R_{C0^*}$ );
- 3 – **class C1**: full spheres touching the lateral walls (coordination number is less/equal than in both classes C0 and C0\*, and  $R_{C0} \geq R_{C1}$ );
- 4 – **class C1\***: partial spheres touching the lateral walls (coordination number is less than in class C0 and C0\*;  $R_{C1} > R_{C1^*}$ );
- 5 – **class C2**: sphere artefacts due to a large volume cut ( $R_{C0} \gg R_{C2}$ );

- 6 – class **C\_other** (not shown in Fig. 4.3): the other spheres touching the top or bottom of the domain if the domain is the entire can (that is to say the X-ray beam scans cover ideally the whole can – it is not the case in this study);
- 7- class **C\_noise** (not shown in Fig. 4.3): residual elements, smaller than the mean connection radius. They can generate incorrect coordination numbers by multi-arc connections (geometrical artefacts in the volume).

Typically there are two different configurations (Fig. 4.4.a-b): non-compressed and compressed spheres (pebbles). To evaluate the main radius value distributions including the different classes and the compression effect, one must take into account only the objects with a radius being nearly the same as the mean radius. The other objects (**C2**, **C\_other** and **C\_noise** classes) are not used to compute the mean values, but they are still considered in the ML graph analysis to characterise the connections and the contact surfaces of the **C0**, **C0\***, **C1** and **C1\*** classes.

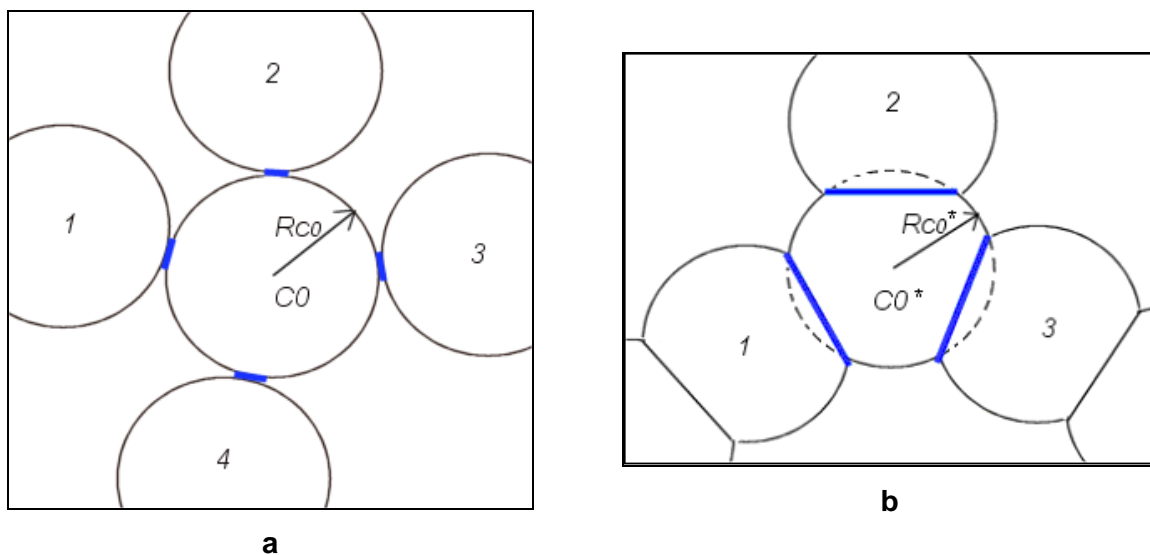


Fig. 4.4. Different pebble configuration cases: a) non-compressed pebbles; and b) compressed pebbles.

### 4.3. Expected Results

The main results shown hereafter refer to:

- 1- **The number of objects** in the volume, i.e. the sum of **C0**, **C0\***, **C1**, **C1\*** and **C2** class elements;
- 2- **The position of object centres** in Cartesian co-ordinates;
- 3- **The object radius frequency** in the volume;

- 4- **Coordination number distribution:** the number of connections for each pebble;
- 5- **Total contact area distribution:** the sum of all connection surfaces associated to the pebbles (s. blue objects in Fig. 4.4.a);
- 6- **Contact area ratio distribution:** i.e. for each object the ratio between the total contact surface area referred to the ideal sphere surface (radius **Rco** in the Fig. 4.4.a);
- 7- **Medial line graph visualisation:** a 3D view of the whole sample.

Most results will be obtained basing on the analysis of the ML graph and the topology of connections. Some compression effects can be understood looking at Fig. 4.4.a-b, where a non-compressed and a compressed pebble configuration are shown.

#### 4.3.1. Compression - Contact Surface Ratio - Coordination Number

In a non-compressed can (Fig. 4.4.a), the mean radius (i.e. the class **C0**) characterises the sphere and its four connections (coordination number = 4). If the compression increases the spheres will be deformed (figure 4.4.b). For small compressions we can argue that the **C0** radius does not undergo a significant reduction (transition to the **C0\*** class), but the contact area increases. Also, we can observe in figure 4.4.b that the coordination number becomes 3 since only three connections are still present. In this case the decrease of the coordination number is associated to a real increase in the surface contact area and contact area ratio (shape index).

#### 4.3.2. Domain location and Edge Effects - Coordination Number

The coordination number denotes a structural parameter related to the internal arrangement of the pebbles. The can edges and the relative sample location in the can affect the structural arrangement. At the bottom of the can, the influence of the can edges is expected to be more important than in the can mid part, thus inducing a change of the mean coordination number.

#### 4.3.3. Class **C2**, **C\_other** and **C\_noise** - Coordination Number

The **C2**, **C\_other** and **C\_noise** object classes will be used to help to determine the coordination number and the contact surface area but they can generate some errors. The most important error can be the increase of the coordination number in some objects due to false arc connections in the volume (long arcs). This overestimation is not expected to be significant with regard to the evaluation of the domain's mean quantity values.

#### 4.4. Post-Processing

As already mentioned above, the main objective of this analysis is the determination of the main radius, the contact area and the coordination number of each object as well as the poloidal angle distribution which can be directly related to the SBZ model contact surface index. The algorithms employed are based on the post-processing of the FML graph representation proposed in [16]. In the next sections is described the main post-processing strategy adopted to evaluate the results presented in Section 2.5.

**Internal ROI determination to exclude object-edge contacts:** An internal ROI has been defined to exclude from the analysis spheres in contact with the can lateral walls and also partial spheres (cut spheres). By that, one detects if a sphere centre (or node in the FML graph) is placed inside the internal ROI, otherwise the node does not count for statistics. In order to obtain the internal ROI radius one must subtract one sphere diameter (the diameter average value is 3.4 (mm)) from the radius of the ROI can. Its height is the height of the ROI reduced by one sphere diameter (taking one radius\* from the top and one from the bottom).

**Connection overhead filter:** A special filter has been developed, called connection overhead filter, which controls that the distance between two connected balls be lower than a maximal distance, otherwise the connection will be labelled as not valid.

**Determination of the contact surface index:** The surface contact index is the sum of all contact surfaces per pebble normalised by the cross section of the pebble.

**Geometric contact surface index – Definition:** The geometric contact surface index [Pieritz, 2004 b], is given by:

$$GeoIndex = \sum_i \frac{(\pi R_c^2)}{(4\pi R_s^2)} \quad (2)$$

where: - i : i-th connection with a pebble;

- R<sub>c</sub>: connection node radius;

- R<sub>s</sub>: pebble (sphere) radius;

This index is representative of the total amount of the spherical surface in contact with other spheres.

## 4.5. Topology Results

### 4.5.1. Post-processed Results

Table 4.1 summarises the main results of the post-processed FML for all samples. The following figures present results for the non-compressed sample S0; the corresponding results for the other samples are given in the Appendix. Figure 4.5 a) contains the final post-processed FML graph representation (main nodes in red and arcs in blue) of a set of 217 pebbles. Figure 4.5 b) shows a perfect sphere representation of the pebble configuration. These pebbles have their centres (main characteristic voxels) inside the post-processed ROI to ensure that they are not in contact with the can walls and the pebbles cut by the ROI boundaries. The resulting configuration represents approximately the height of one and a half slice in the original pebble network.

Table 4.1. Main results of the post-processed FML for all samples.

Sample	S0	S1	S6mid	S6bot
Compression (MPa)	0	8	16	16
Total No of objects	518	458	404	564
No of objects (Classes C0, C0*, C1 and C1*)	348	244	225	295
No of analysed objects (Class C0)	217	137	114	198
Average radius (m)	1.69	1.68	1.68	1.69
standard deviation (m)	0.02	0.02	0.02	0.02
Average coordination No per sphere	6.35	6.53	6.19	5.86
standard deviation	0.23	0.89	0.77	0.58
Average contact area per sphere (mm <sup>2</sup> ) standard deviation (mm <sup>2</sup> )	2.16 1.36	3.07 9.72	6.48 1.12	5.92 1.62
Average geometric contact surface index (%)	2.33	6.41	15.74	13.47
standard deviation (%)	0.14	1.54	3.07	4.30
Average contact surface index (%)	0.712	2.01	4.79	4.60
standard deviation (%)	0.04	0.56	0.47	1.29

Figure 4.6 shows the distribution of the coordination number by frequency (in red bars) and of the pebble average radius (green bars) as a function of the coordination number  $N_c$ . The average value of  $N_c$  is 6.3, compare Table 4.1, the average pebble radius is not dependent on  $N_c$ . More detailed discussions of  $N_c$  will be presented in Section 4.5.4.

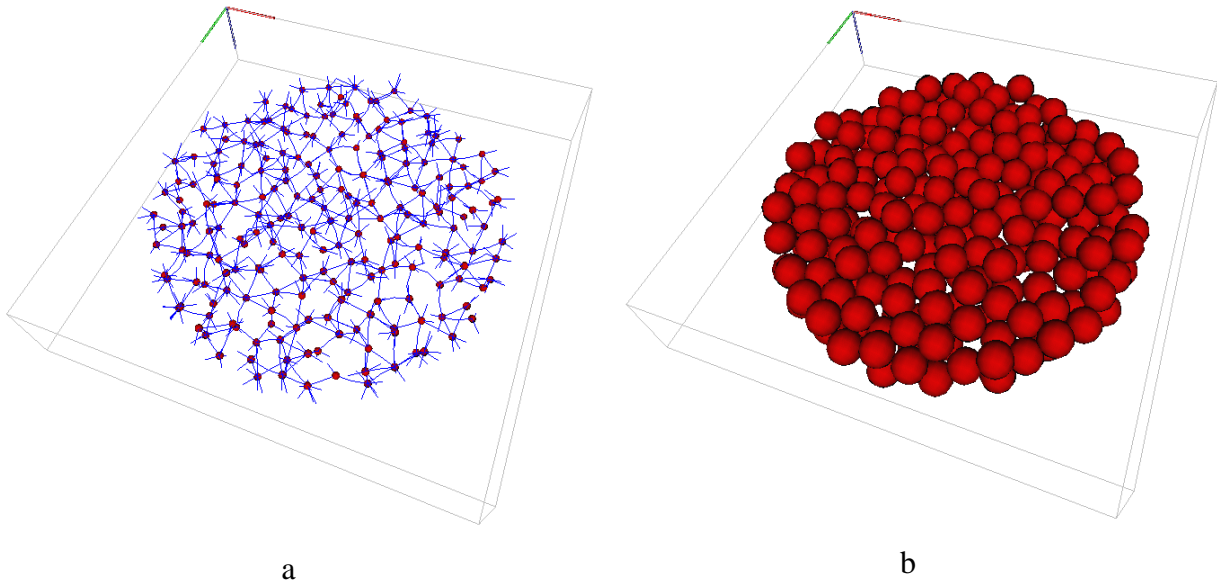


Fig. 4.5 a) FML graph view, b) 3D view of the analysed pebbles (217 objects) of sample S0.

Figure 4.7 shows that the average coordination number does not depend on the pebble radius. The post-processing evaluation came up with the result that only 5 radius size pebble classes are present in the sample, namely: 1.6688, 1.68, 1.6912, 1.7024 and 1.7136 [mm]. The average radius value shown is 1.6887 [mm], with a standard deviation of  $3.5 \times 10^{-3}$  [mm]. This radius represents the maximum inscribed sphere – the maximum internal radius without surface effects (irregularities e.g. departures from ideal sphericity).

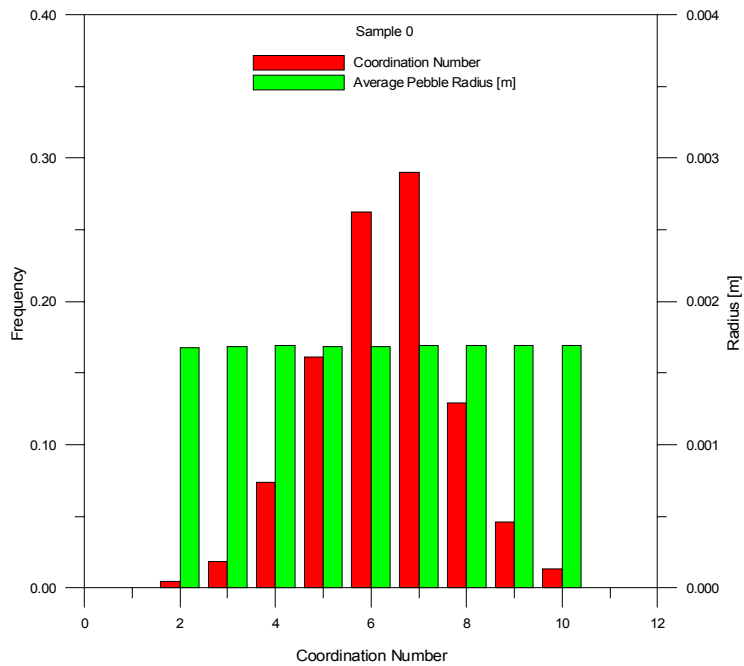


Fig. 4.6. Coordination number (red bars) and pebble average radius distribution (green bars) in sample S0.

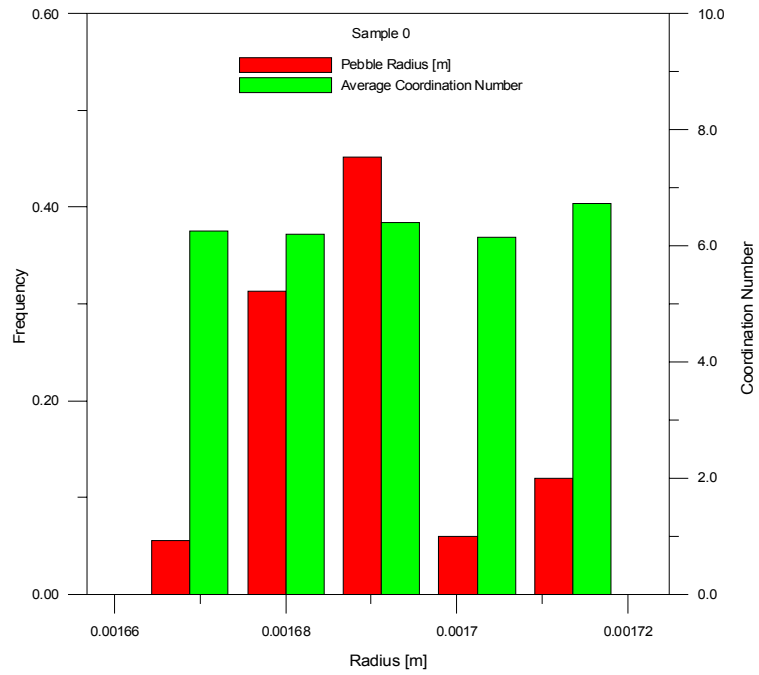


Fig. 4.7. Pebble radius size distribution frequency (red bars) and average coordination number vs. pebble radius (green bars) for sample S0.

Figures 4.8 and 4.9 show the fraction of the pebbles surface in contact with other pebbles, respectively for the SBZ index and the geometric contact index (Section 4.4 - Eq. 2, spherical surface in contact with other pebbles).

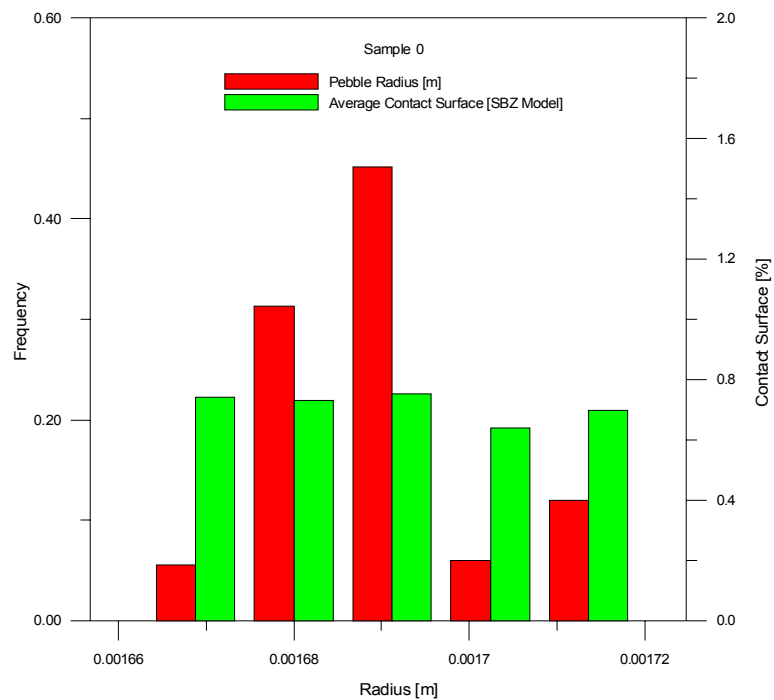


Fig. 4.8. SBZ Contact surface index and pebble radius size distribution frequency (in green) for sample S0.

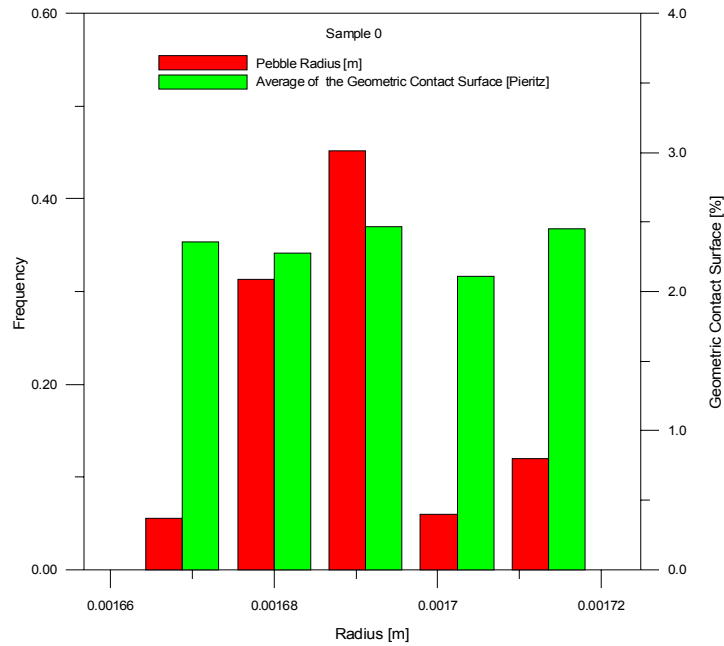


Fig. 4.9. Geometric contact surface index by pebble radius size distribution frequency for sample S0.

#### 4.5.2. Sphere Positions

As mentioned above, the MLG ROI, used for the topological analyses, is smaller than the ROI used in Section 3, see Fig. 3.1. Because of this, the spheres adjacent to the cylindrical wall (1<sup>st</sup> row) are excluded as well as the spheres in the 1<sup>st</sup> bottom layer adjacent to the bottom plate.

Figure 4.10 depicts the horizontal positions of the sphere centres for all samples. This figure shows also the circles where the sphere centres of the 1<sup>st</sup>, 2<sup>nd</sup> and 3<sup>rd</sup> rows should be located assuming a dense hexagonal packing neglecting the influence of curvature, compare [Benenati,1961]: The radius of the first row is 22.75mm; the radii of the next circles differ by 0.82 d. The figure shows that the sphere centres of the second row are quite close to the corresponding circle and even a regular structure in the zone of the 3<sup>rd</sup> row is still observable.

There are also sphere centres at radii larger than that for the 2<sup>nd</sup> row. This is due to imperfections (blanks) in the 1<sup>st</sup> row.

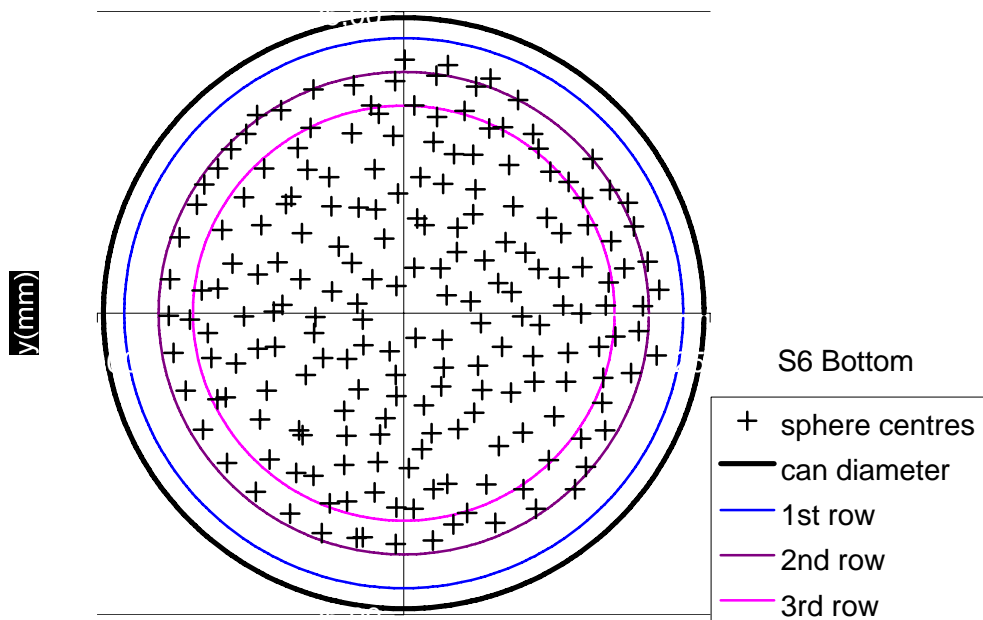
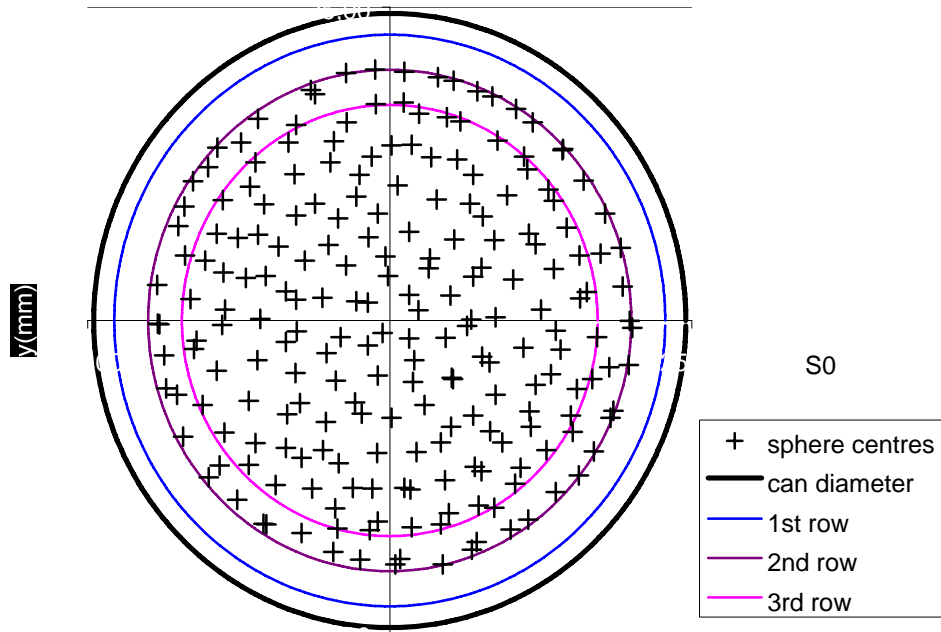


Fig. 4.10. Horizontal positions of sphere centres.

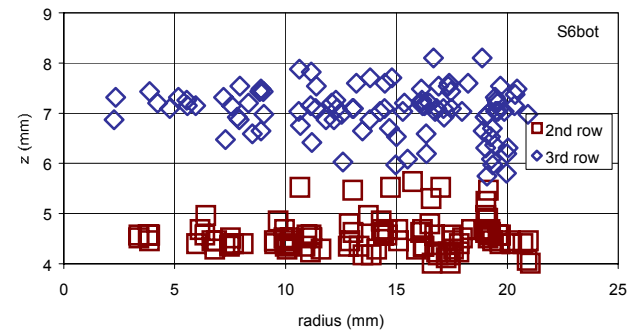
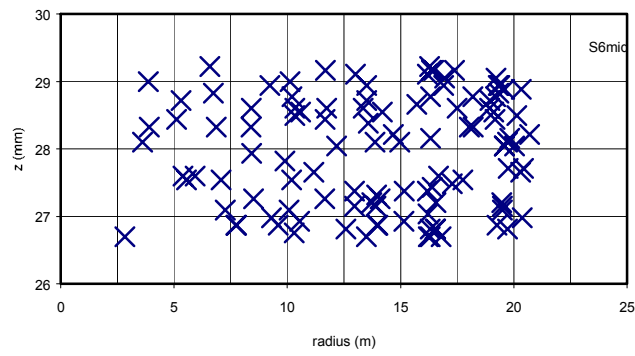
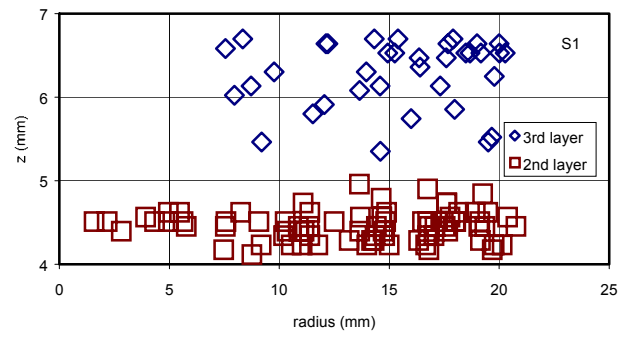
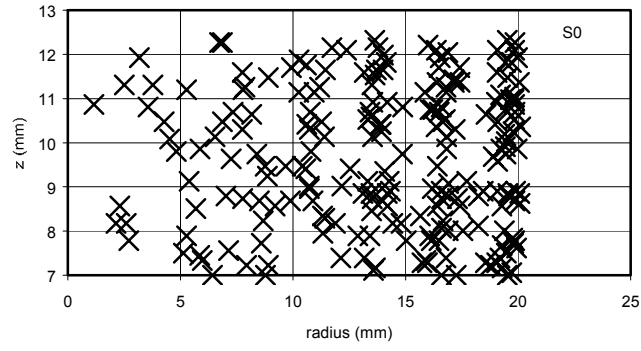


Fig. 4.11. Vertical positions of sphere centres.

The radial, and, additionally, the vertical structure are exhibited by plotting the sphere centres in a map with the vertical distance from the bottom  $z(\text{mm})$  and the radius  $r(\text{mm})$  as co-ordinates, see Fig. 4.11. Again, the 2<sup>nd</sup> row is clearly detectable in all samples. For S1 and S6bot, the vertical structure is also well expressed: the distance between 2<sup>nd</sup> and 3<sup>rd</sup> layer is again  $\approx 2.8$  mm.

#### 4.5.3. Contact Surfaces

Figure 4.12 shows for all samples the distribution of the contact surfaces  $A_c$  normalised with the sphere cross section  $A$ . The first group contains the data between 0 and 1%, the second between 1 and 2%, etc. In the first group, nearly all data have the value of 0.11% which corresponds to the smallest possible detectable contact surface with a diameter of about 3 voxels. These surfaces are so small that they can be interpreted as point contacts. Figure 4.13 shows the distribution for Sample S0 with a higher resolution. For the non-compressed bed S0, ideally all contacts should be point contacts. Therefore, the unexpected group with values between 2 and 3 % asks for special interpretation.

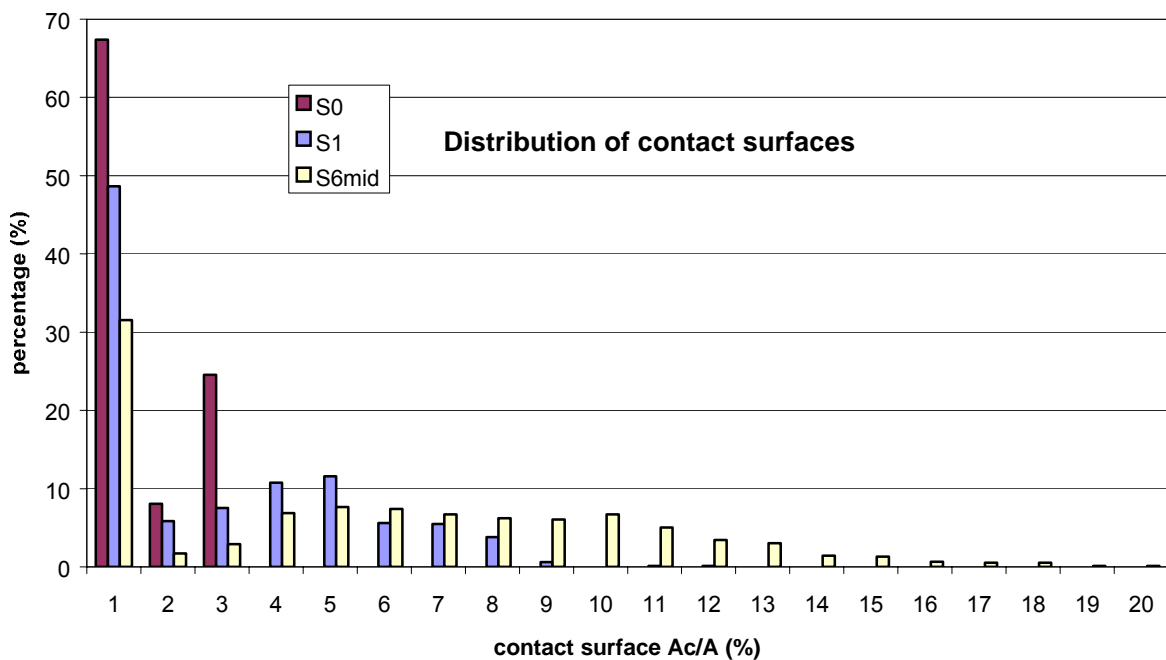


Fig. 4.12. Distribution of normalised contact surfaces.

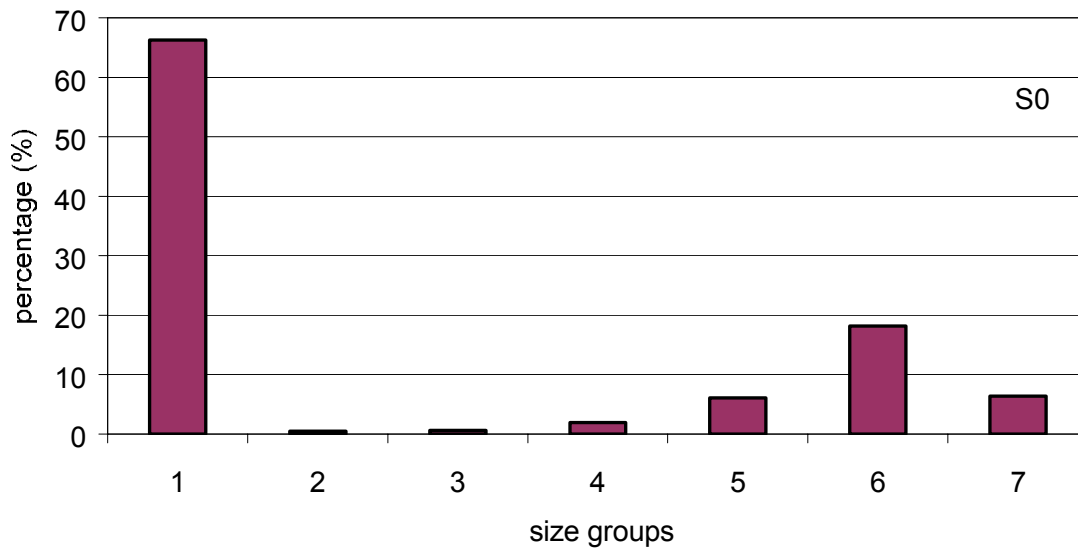


Fig. 4.13. Details of contact surface distribution for S0: (group/ $A_c/A$ (%): 1/0.01; 2/(>0.01-0.5); 3(0.5-1.0); 4/(>1.0-1.5); 5/(>1.5-2.0); 6/(>2.0-2.5); 7/(>2.5-3.0)).

This special group of contact surfaces might have been generated during the vibration assisted filling process. However, the following arguments suggest that this is not the case: in all previous experiments, compare e.g. [1-3], the beds were filled in the same way. As mentioned in Section 2.1, the measured thermal conductivity for non-compressed beds agrees fairly well with predictions from the SBZ model [4] for values  $A_c/A$  between  $10^{-2} - 10^{-1}$  %. For a value  $A_c/A = 2\%$ , the SBZ model predicts a conductivity value for the aluminium pebble bed in helium, see Fig. 2.3 which is larger by a factor of 15 than the value for non-compressed beds. Although the SBZ model might not be physically correct in all details, it should not be wrong by orders of magnitudes in respect to  $A_c/A$ .

Presently, the following explanation appears to be most plausible: the aluminium spheres are not ideally spherical: diameter measurements using the same sphere showed variations of  $\pm 25\mu\text{m}$ . In order to define mathematically spherical objects, the maximum possible sphere is defined inside the measured objects. This results in sphere diameters smaller than 3.5mm; in fact, the mean sphere diameter determined was to be 3.4mm. The volume outside then gives rise to contact surfaces as an artefact. Other possibilities are: errors from signal correction (volume image operations + threshold and filters operators + etc), image connectivity uncertainty due mathematical connectivity choice (number of active neighbours of the voxel), numerical error in operators, and the REV (Representative Elemental Volume) problem (Representative Elemental Volume)

Figures 4.12 and 4.13 show that with increasing compression the number of contact surfaces with  $A_c/A=0.11$  decreases and the contact surfaces shift to larger values. For S1, a maximum occurs at  $A_c/A \approx 5\%$  and for S6 a broad plateau exists with values between 4 and 10%. An open question is if/how the questionable smallest contacts become physical meaningful contacts for compressed beds.

Figure 4.14 contains for S0 the distribution of contact surfaces for the individual spheres sorted in such a way that the largest value is attributed to contact number 1, the second largest contact to  $n = 2$  etc. Additionally, the fraction of the values  $A_c/A = 0.1$  in each group is listed. 8.5% of all spheres have only contacts with  $A_c/A = 0.1$ ; 64% of all spheres have two contacts larger than 0.1% and all contact numbers larger than 6 have values of  $A_c/A = 0.1$ . Figure 4.15 contains corresponding results for S1. There are no longer spheres with only contacts of  $A_c/A = 0.1$ .

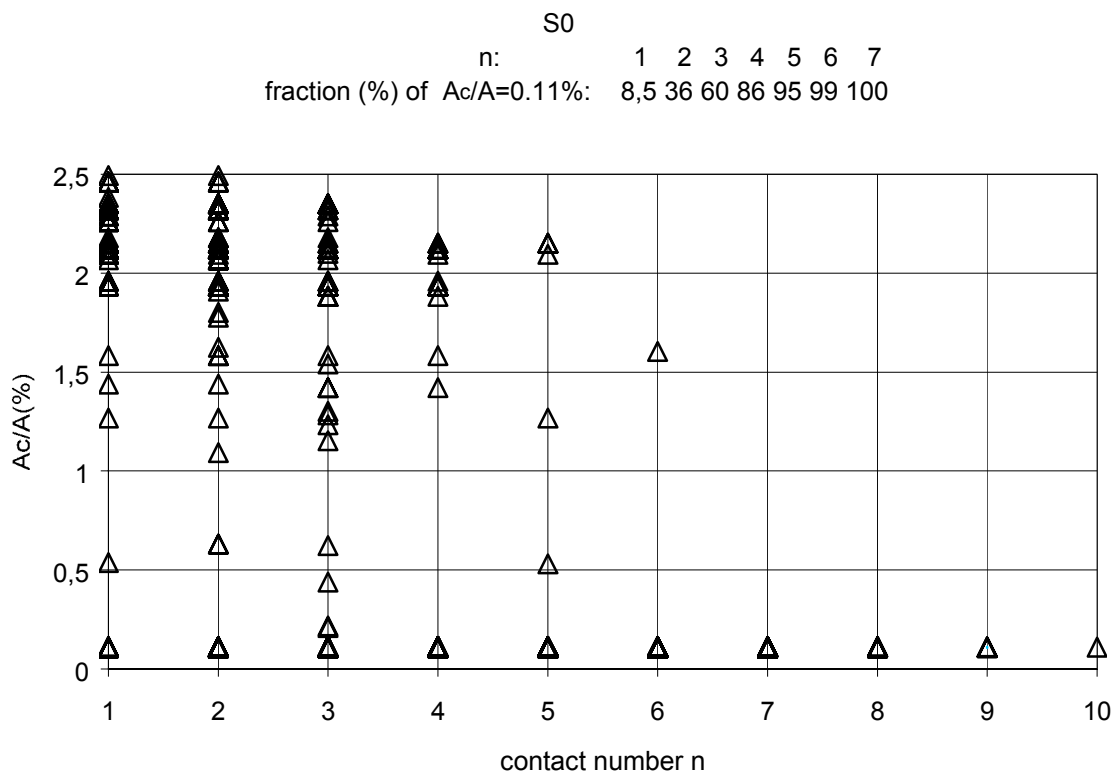


Fig. 4.14. Contact surface distribution on the spheres (sample S0).



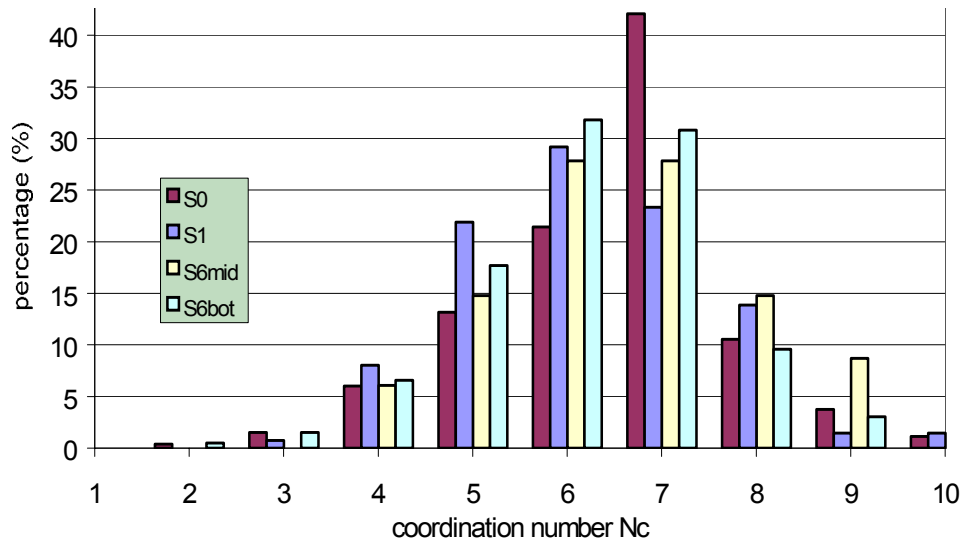


Fig. 4.18. Distribution of coordination numbers for all samples.

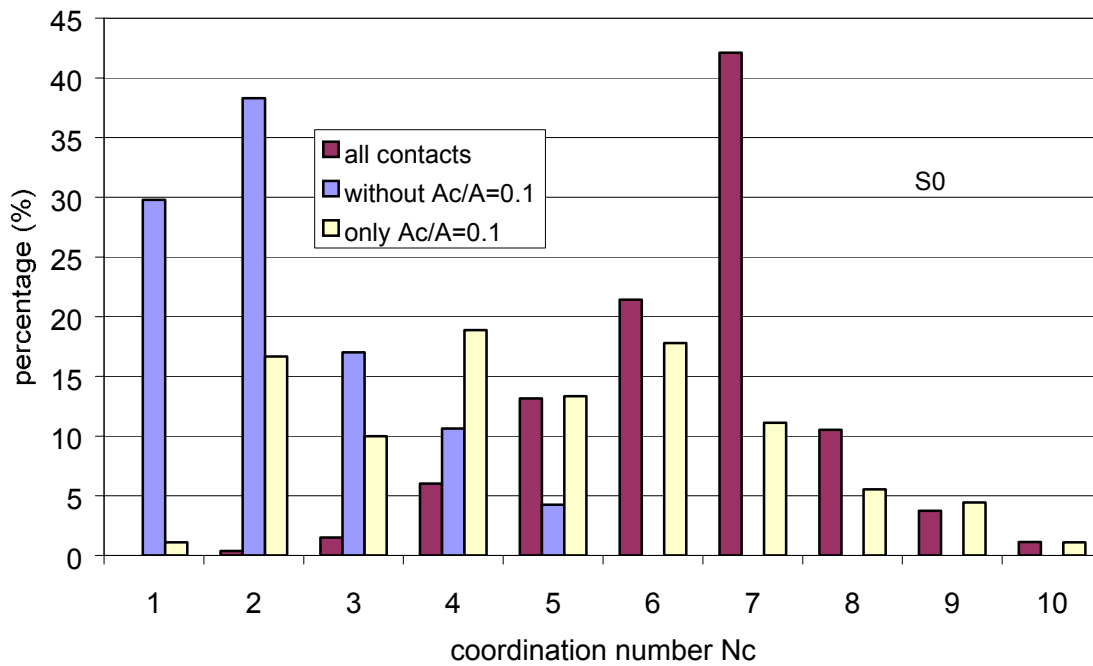


Fig. 4.19. Detailed distribution of coordination numbers for sample S0.

Figure 4.18 shows the determined coordination numbers  $N_c$  for all samples. The maximum values are between 6 and 7, which is in good agreement with other work [25]. The present experiments show no remarkable influence of deformation on  $N_c$ .

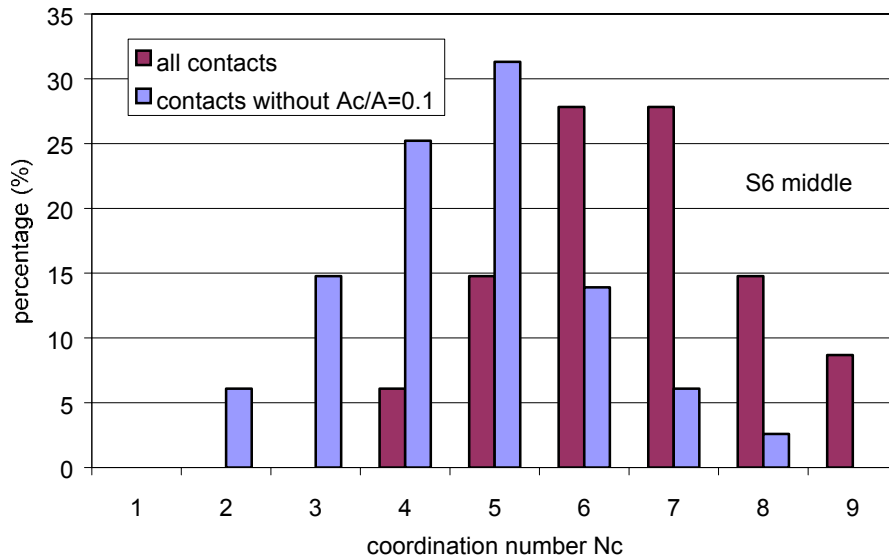


Fig. 4.20. Detailed distribution of contact numbers for sample S6mid.

Again, it is of interest to analyse in more detail sample S0. Figure 4.20 depicts the coordination numbers for the cases: a) all contacts, b) without the contacts  $A_c/A=0.11$ , c) using only the contacts  $A_c/A=0.11$ . Neglecting the contacts  $A_c/A=0.11$  results in unreasonable values of  $N_c$ . Neglecting the large contact values, again the distribution is shifted to such low values that the data appear to be not physically meaningful. Only the use of all contacts gives the agreement with other data. The same tendencies is observed for sample S6mid, the number of contacts  $A_c/A=0.11$  is smaller compared to S0; therefore, the tendency is less expressed but still existent, see Fig. 4.20.

#### 4.5.4. Poloidal Distribution of Contact Surfaces

In UCTs, the pebble beds are subjected to a pressure in the vertical direction. The important question, therefore, is if this can be also seen in the angular distribution of contact surfaces  $A_c/A$ . Figure 4.21 shows  $A_c/A$  as a function of the poloidal angle  $\delta$  (starting with 0 at the “North Pole”). For uncompressed beds, there is no significant dependence from poloidal angle (the agglomeration of data in the zone close to  $\delta = 90^\circ$  is caused by the fact that sphere surface increments are largest there). However, again the existence of two groups of data is pronounced: one group with  $A_c/A = 0.1$  and the other with  $A_c/A \approx 2.2$ . For compressed beds there is the clear tendency that the largest values concentrate in zones with  $\delta \leq 45^\circ$  and  $\delta \geq 145^\circ$ , i.e. in zones where the contact surfaces are predominantly perpendicular to the uniaxial stress.

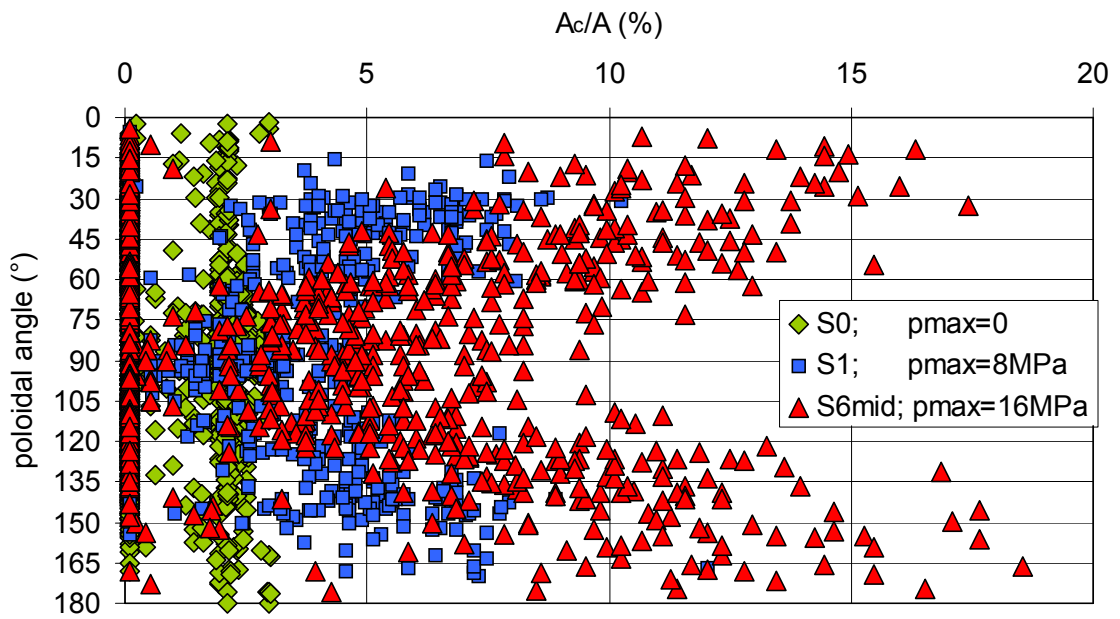


Fig. 4.21. Poloidal distribution of contact surfaces on the spheres.

For the spheres closest to the bottom (2nd bottom layer of samples S1 and S6bot) the packing is expected to be close to the hexagonal dense packing structure with contacts at  $\delta \approx 35^\circ$ ,  $90^\circ$  and  $\approx 145^\circ$ . If only spheres are considered at radial positions smaller than 15mm in order to avoid disturbances coming from the cylindrical wall, this tendency is well expressed, as shown in Fig. 4.22.

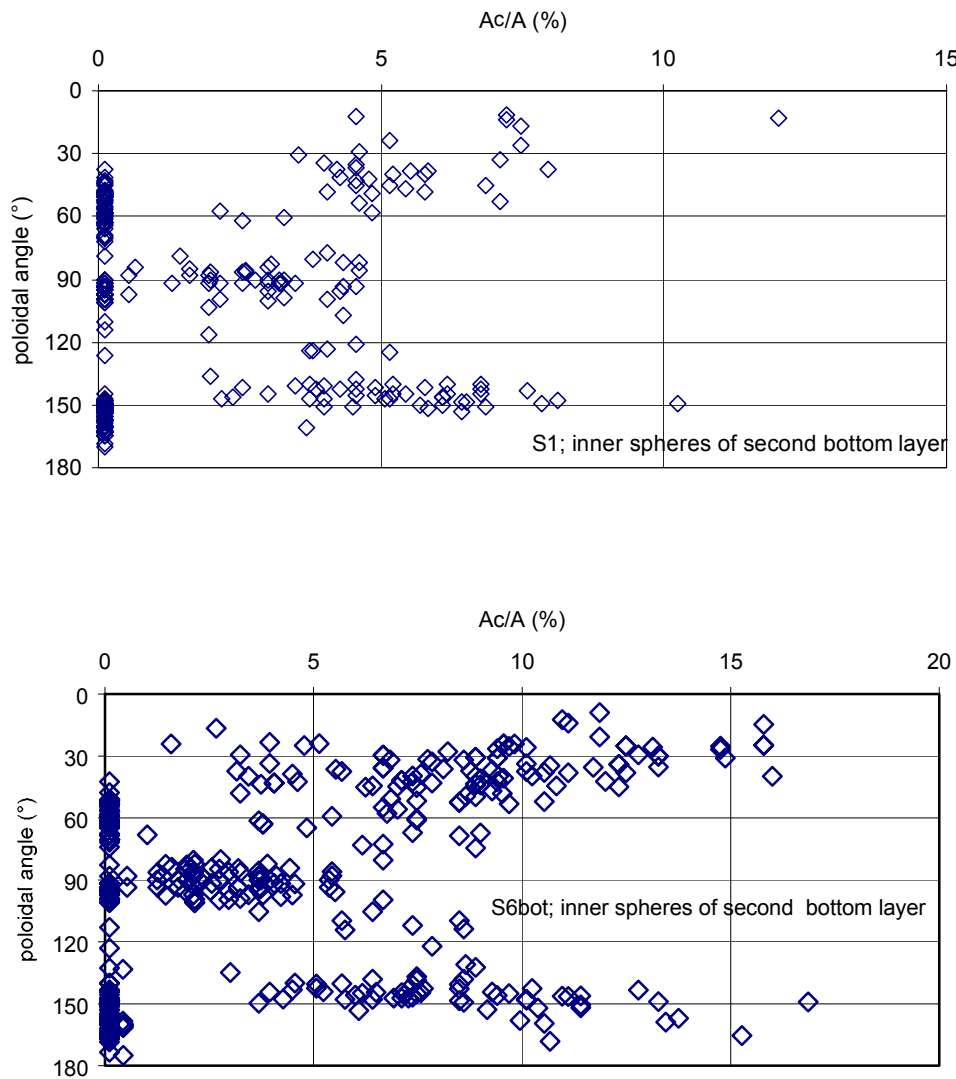


Fig. 4.22. Poloidal distribution of contact surfaces on the inner 2<sup>nd</sup> bottom spheres for samples S1 and S6bot.

## 5. FUTURE EXPERIMENTS

The experiments described in this report are considered as a first step of a larger programme to investigate the topology of compressed pebble beds. In the future, the following investigations will be performed (ESRF contract No ME 898):

- Calibration of contact surfaces: individual aluminium spheres will be deformed between steel plates with different forces and the contact surfaces will be measured by optical microscopy. The contact surfaces determined by tomography will be compared with the expected contact surfaces according to the maximum pressure in the UCT.

- Comparison of data with experiments where topological data were measured by microscopy, compare [6]. The detailed data evaluation of the latter experiments is underway. These data will be very useful in respect to the comparison of coordination numbers and contact surfaces.
- New measurements of thermal conductivity of compressed pebble bed in HECOP-facility.
- Performance of further microtomographical with pebble beds consisting of 2.3mm aluminium spheres contained in cans of the same dimensions as in the present investigations. During scanning, the spatial resolution will be increased by a factor of two. Besides the quantities presented in this report, the following additional quantities will be determined:
  - contact surfaces between spheres and cylindrical/bottom walls,
  - azimuthal distribution of contact surface on the spheres,
  - scans over the total height of the samples in order to obtain statistically relevant data on void fraction distributions.

## 6. CONCLUSIONS

Microtomography has proven to be a unique technique to determine inner structures of pebble beds. This technique has been applied for the first time to detect coordination numbers, contact surfaces and their positions on spherical pebbles. It has been demonstrated that in uniaxial compression tests (UCTs), which are standard tests for the characterisation of thermal-mechanical properties of pebble beds, the poloidal distribution of contact surfaces is non-homogeneous. Therefore, the data generated in general by UCTs (modulus of deformation, thermal creep correlations) must be critically reviewed in respect to the extrapolation to blanket applications.

There are some remaining open questions in respect to the accuracy of the results concerning the determined contact surfaces. These issues will be investigated in the next experiments.

The final goal of the joint FZK-ESRF investigations is the improvement of heat transfer models to describe the thermal conductivity of pebble beds and the heat transfer coefficient between pebbles and walls. This goal requires the accurate knowledge of topological quantities and will be addressed in the future.

## REFERENCES

- [1] J. Reimann, L. Boccaccini, M. Enoeda, A. Y. Ying, Thermomechanics of solid breeder and Be pebble bed materials, ISFNT-6, San Diego, USA, April 7-12, 2002, Fusion Engineering and Design, 61-62, 2002, pp. 319-331.
- [2] J. Reimann, G. Piazza, Z. Xu, A. Goraieb, H. Harsch, Measurements of the Thermal Conductivity of Compressed Beryllium Pebble Beds, Forschungszentrum Karlsruhe, FZKA 7096, 2005.
- [3] J. Reimann, G. Piazza, H. Harsch, Thermal conductivity of compressed beryllium pebble beds, 7<sup>th</sup> Int. Symp. Fusion Nucl. Techn., Tokyo, Japan, May 22-27, 2005.
- [4] E.V. Schlünder, Particle heat transfer, Proc. 7th Int. Heat Transfer Conf. München, Germany, Washington: Hemisphere Publ. Co., Vol. 1, RK 10, 1982, pp. 195-212.
- [5] J. Reimann, R. A. Pieritz, M. di Michiel, C. Ferrero, Inner structures of compressed pebble beds determined by X-ray tomography, Proceedings of the 23rd Symposium Fusion Technology, Venice, Italy, 20-24 Sept. 2004, Fusion Engineering and Design, in press.
- [6] J. Reimann, R. A. Pieritz, R. Rolli; Topology of Compressed Pebble Beds, 7<sup>th</sup> Int. Symp. Fusion Nucl. Techn., Tokyo, Japan, May 22-27, 2005.
- [7] P. Falus, M. A. Borthwick, S. G. J. Mochrie, Rev. Sci. Instrum., **75**, 4383, 2004.
- [8] E. Zych, C. Brecher and J. Glodo, J. Phys. Condensed Matter **12**, 1947, 2000.
- [9] <http://www.esrf.fr/UsersAndScience/Experiments/TBS/InstrumentSupport/ISGUnits/ControlElectronics/Projects/OPIOM/>.
- [10] A. C. Kak, M. Slaney, Principles of Computerized Tomographic Imaging, page 186, IEEE Press, New York, USA, 1988.
- [11] J. Serra, Image analysis and mathematical Morphology, Academic Press Limited, London, 1982.
- [12] F. Flin, R. A. Pieritz, J. B. Brzoska, B. Lesaffre, C. Coléou, Full 3D Modelling Of Curvature-Dependant Metamorphism: First Results And Comparison With Experimental Tomographic Data, Journal of Physics D: Applied Physics, 36 A49-A54, 2003.
- [13] F. Flin, R. A. Pieritz, J. B. Brzoska, D. Coeurjolly, B. Lesaffre, C. Coléou, P. Lamboley, O. Teytaud, G. Vignoles, J. F. Delesse, Adaptive Estimation of Normals and Surface Area for Discrete 3-D Objects: Application to Snow Binary Data from X-Ray Tomography, IEEE Trans. on Image Processing, Vol. 14, No. 5, May 2005, pp. 585-596
- [14] J-M. Barnola, R. A. Pieritz, C. Goujon, P. Duval, E. Bollor, 3D Reconstruction of the Vostok Firn Structure by X-Ray Tomography, XIII Glaciological Symposium, St.Petersburg, Russie, 2004.

- [15] R. A. Pieritz, Development of The Medial Line Graphics And The Connected Region Threshold Techniques Applied To The Geometrical Porous Media Characterization, Master in Sciences and in Engineering Thesis, Federal University of Santa Catarina, Department of Mechanical Engineering – Brazil, 1994.
- [16] R. A. Pieritz, Modélisation Et Simulation De Milieux Poreux Par Réseaux Topologiques, Doctor Degree Thesis, Université Joseph Fourier, Grenoble I, France, 1998.
- [17] L. H. S. Roblee, R. M. Baird, J. W. Tierney, Radial Porosity Variations in Packed Beds, A.I.Ch.E. Journal, Vol. 4, 1958, pp. 460-464.
- [18] R. F. Benenati, C. B. Brosilow, Void Fraction Distribution In Beds Of Spheres, A.I.Ch.E. Journal, Vol. 8, 1961, pp. 460-464.
- [19] S. Debbas, H. Rumpf, On The Randomness Of Beds Packed With Spheres Or Irregular Shaped Particles, Chemical Engineering Science, Pergamon Press, Oxford, Vol. 21, 1966, pp. 583-607.
- [20] K. Ridgway, K. J. Tarbuck, Voidage Fluctuations in Randomly-Packed Beds of Spheres Adjacent to a Containing Wall, Chemical Engineering Science, Pergamon Press, Oxford, Vol. 23, 1968, pp. 1147-1155.
- [21] H. Martin, Low Peclet Number Particle-to-fluid Heat and Mass Transfer in Packed Beds, Chemical Engineering Science, Pergamon Press, Oxford, Vol. 33, 1978, pp. 913-919.
- [22] O. Bey, G. Eigenberger, Fluid flow through catalyst filled tubes, Chem. Eng. Science, Vol. 52, No. 8, pp. 1365-1376, 1997.
- [23] F. Scaffidi-Argentina, G. Piazza, A. Goraieb, E. Boller, A. Elmoutaouakkil, C. Ferrero, J. Baruchel, Non destructive three dimensional analysis of the packing of a binary beryllium pebble bed, Fus. Eng. and Design, 58-59, 2001, pp. 707-712.
- [24] R. A. Pieritz, J. B. Brzoska, F. Flin, B. Lesaffre, C. Coléou, From Snow X-Ray Microtomograph Raw Volume Data To Micromechanics Modelling: First Results, Annals of Glaciology - International Glaciological Society, Vol 38, 2004.
- [25] J. Bernal, J. Mason; Co-ordination of randomly packed spheres, Nature, Vol. 188, Dec.10, 1960, pp 910-911.

**ANNEX 1**

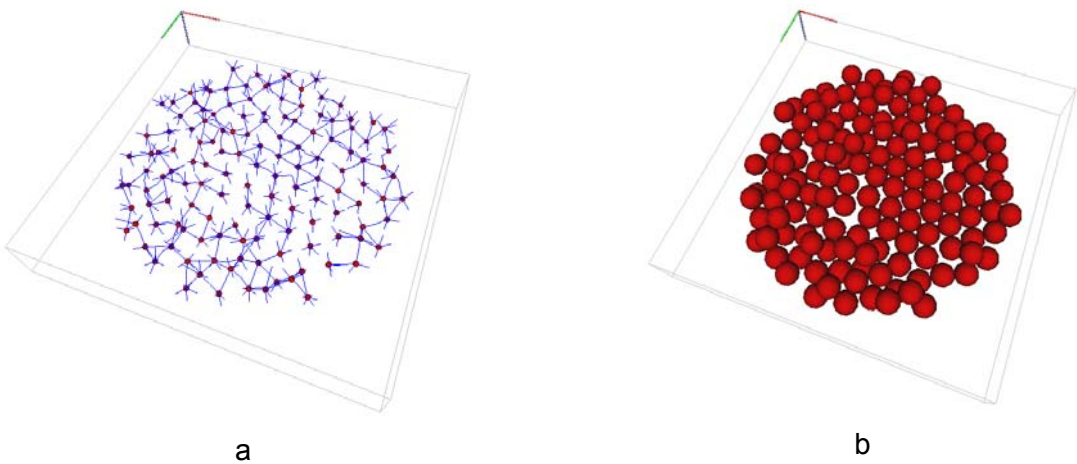


Fig. A.1 a) ML graph view, b) 3D view of the analysed pebbles (137 objects) ; sample S1

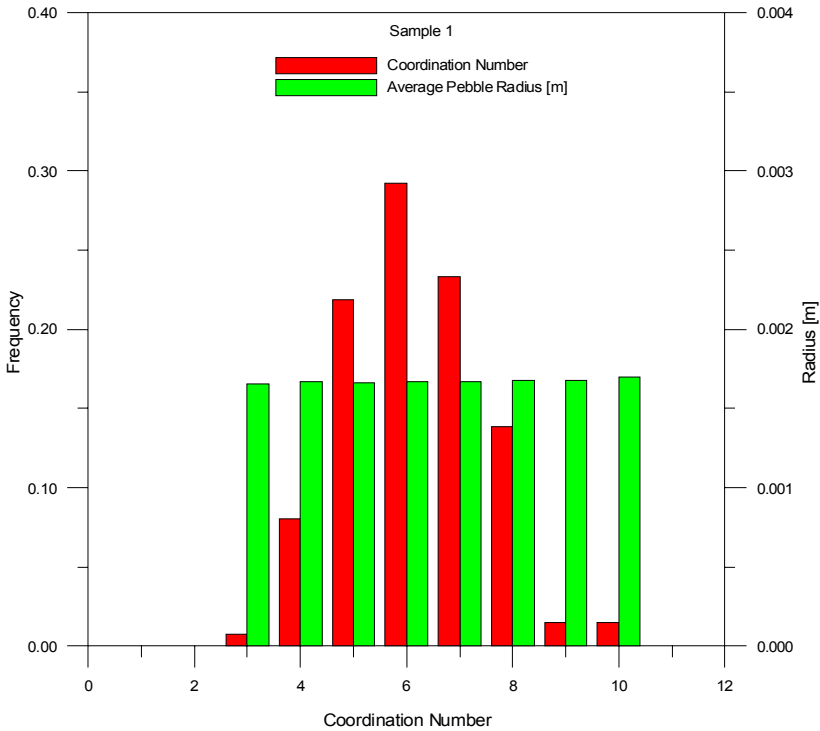


Fig. A.2 – Coordination number (red bars) and pebble average radius (green bars) distribution for sample S1.

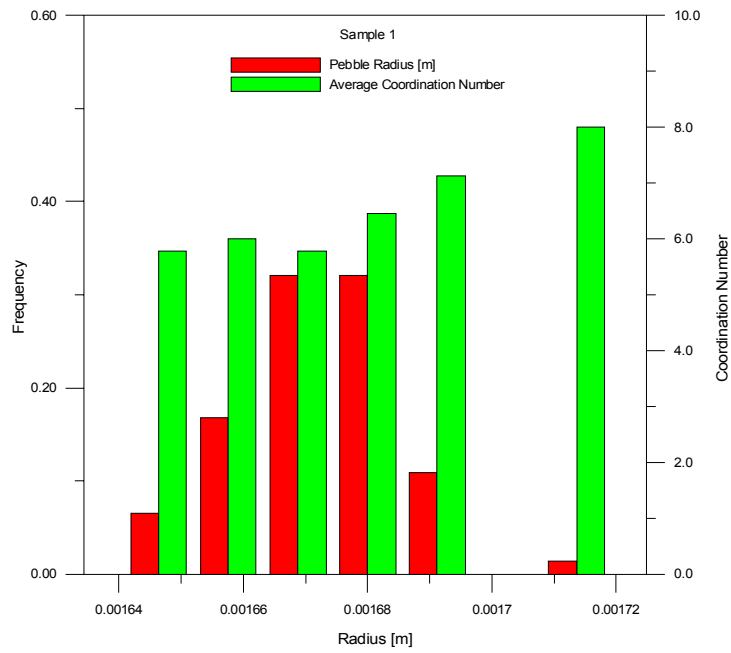


Fig. A.3 – Pebble radius size distribution frequency (red bars) and average coordination number vs. pebble radius (green bars) for sample S1

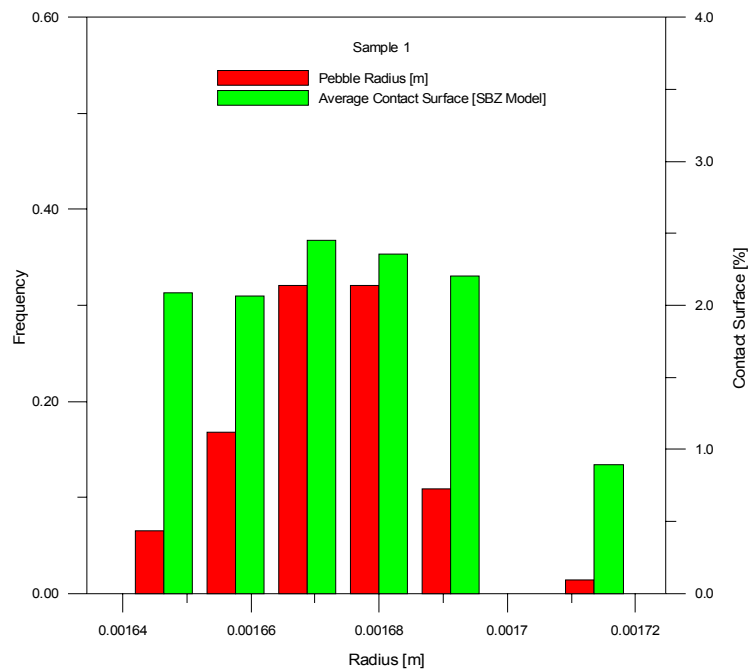


Fig. A.4 – SBZ model contact index by pebble radius size distribution frequency (in green) for sample 1

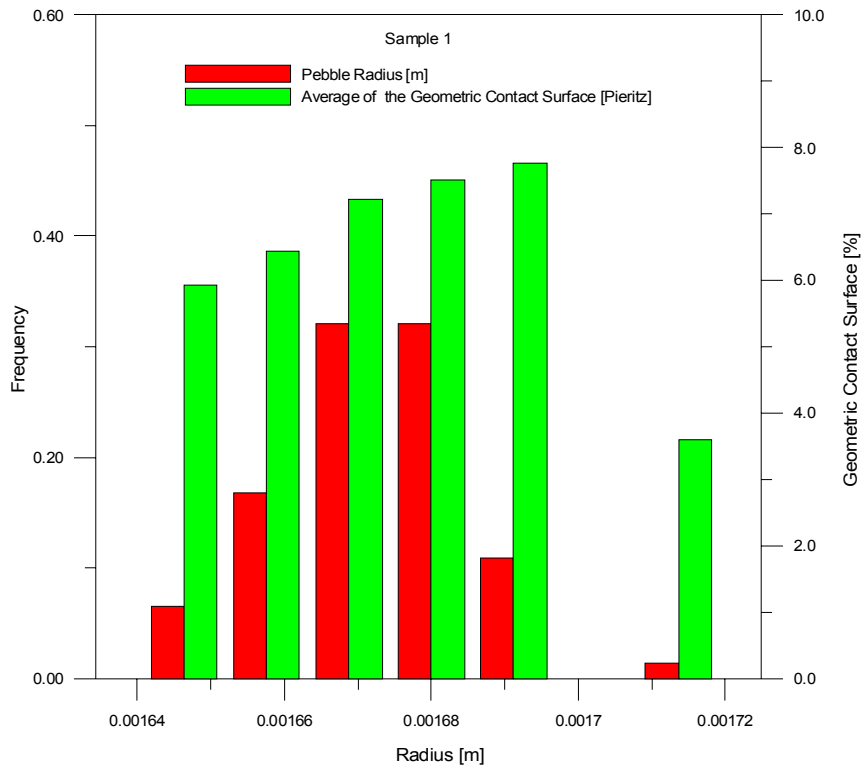


Fig. A.5 – Geometric contact surface index (as defined in section 4.4) by pebble radius size distribution frequency for sample 1

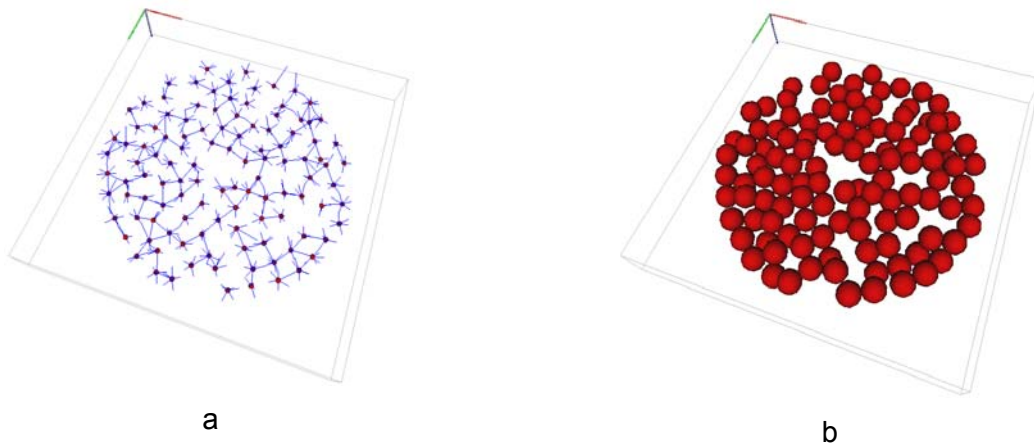


Fig. A.6 – a) ML graph view and b) 3D view of the analysed pebbles (114 objects) of sample S6 - middle

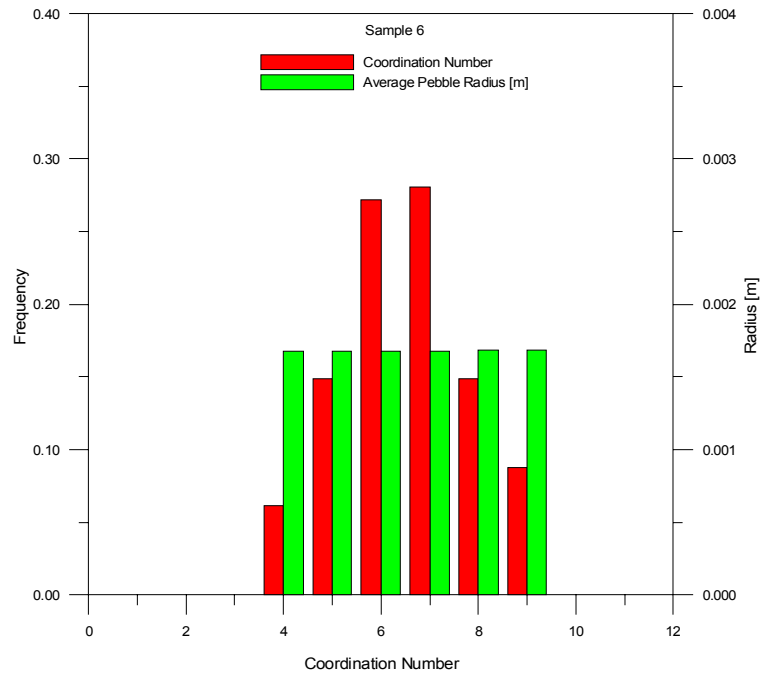


Fig. A.7 – Coordination number (red bars) and pebble average radius (green bars) distribution in sample S6 middle

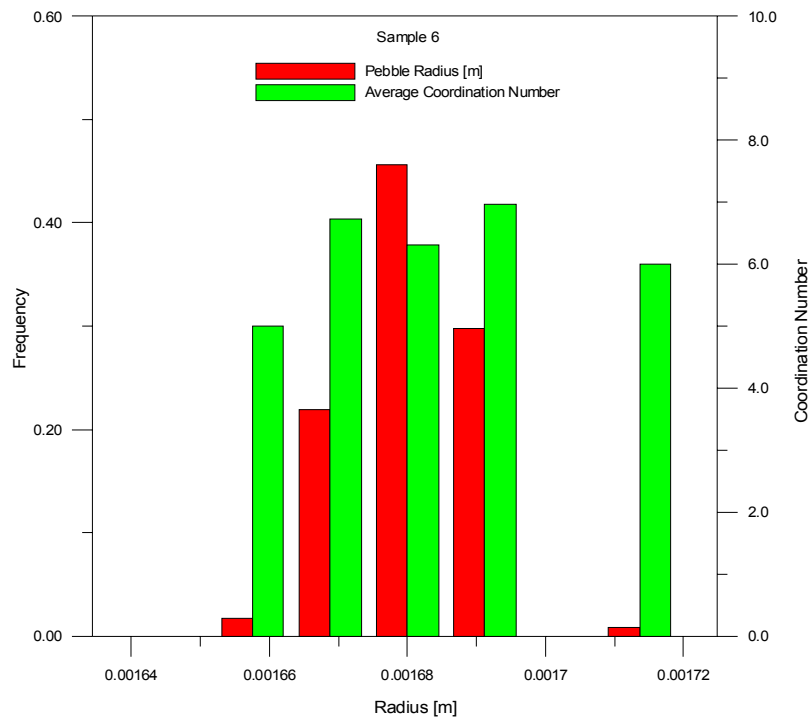


Fig. A.8 – Pebble radius size distribution frequency (red bars) and average coordination number vs. pebble radius (green bars) sample S6 - middle

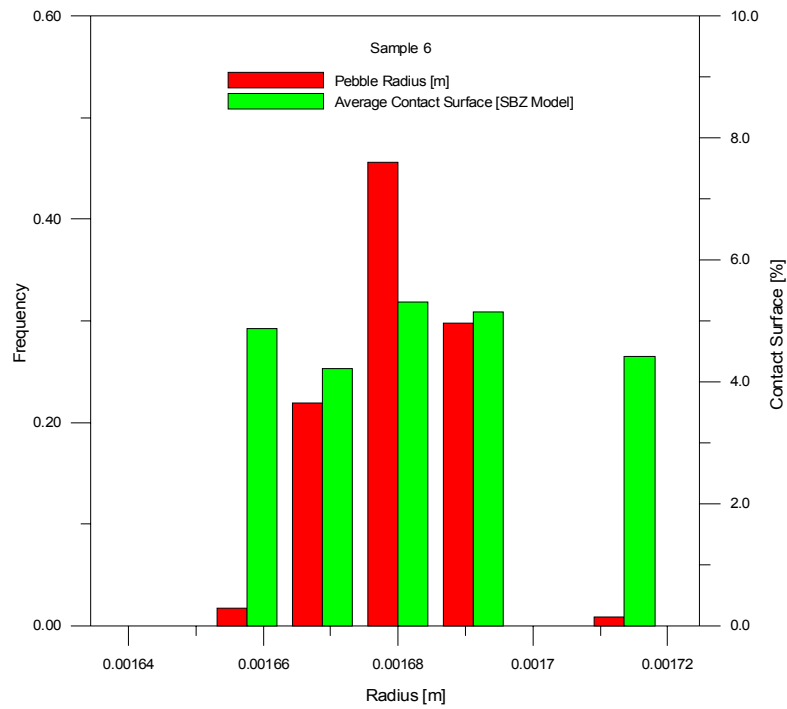


Fig. A.9 – SBZ model contact index by pebble radius size distribution frequency (in green) for sample 6 - middle

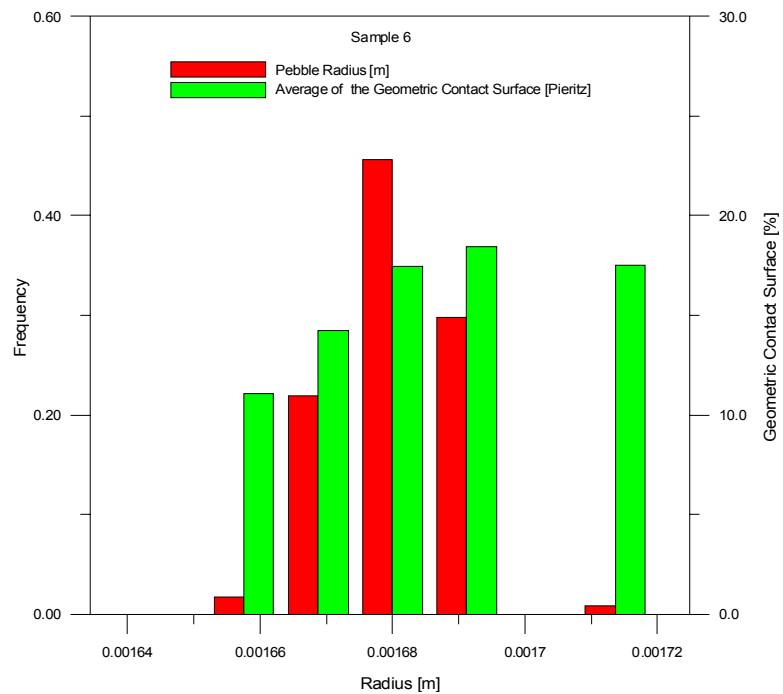


Fig. A.10 – Geometric contact surface index (as defined in Section 4.4)) by pebble radius size distribution frequency for sample 6 - middle

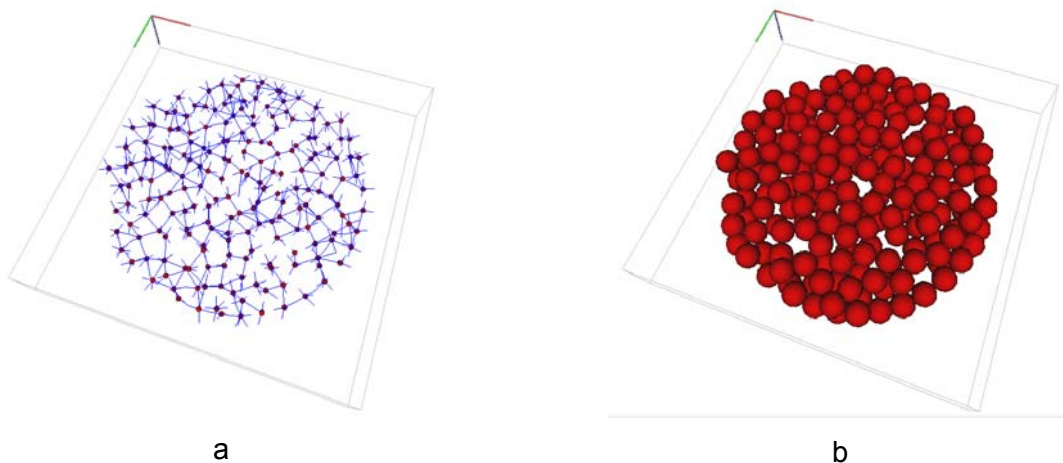


Fig. A.11 – a) ML graph view and b) 3D view of the analysed pebbles (198 objects) of sample S6 - bottom

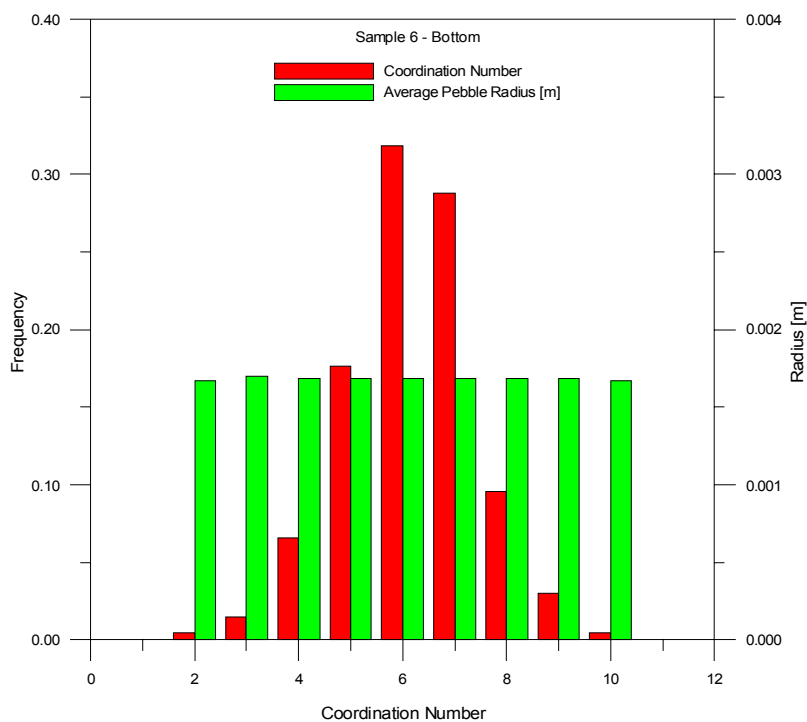


Fig. A.25 – Coordination number (red bars) and pebble average radius (green bars) distribution in sample S6 - bottom

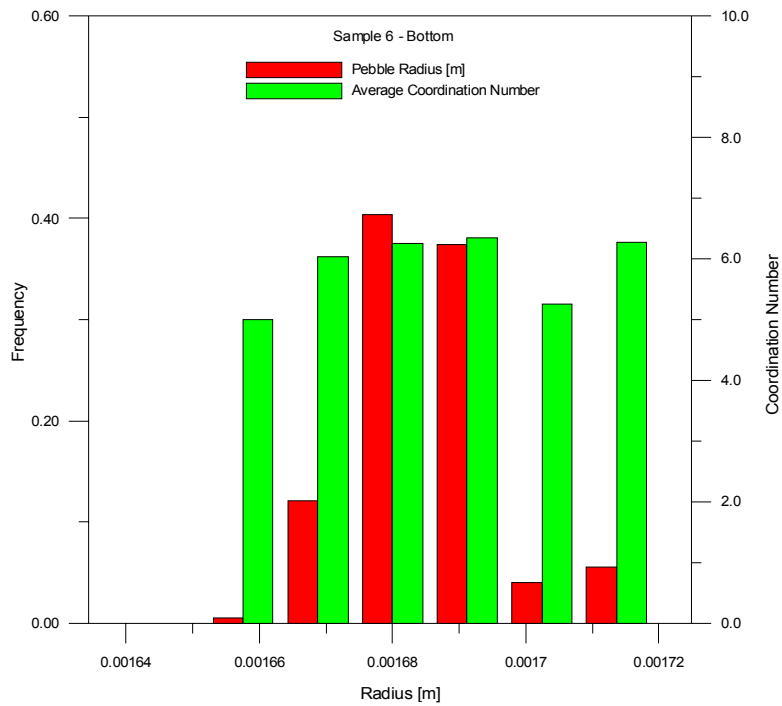


Fig. A.12 – Pebble radius size distribution frequency (red bars) and average coordination number vs. pebble radius (green bars) for sample S6 - bottom

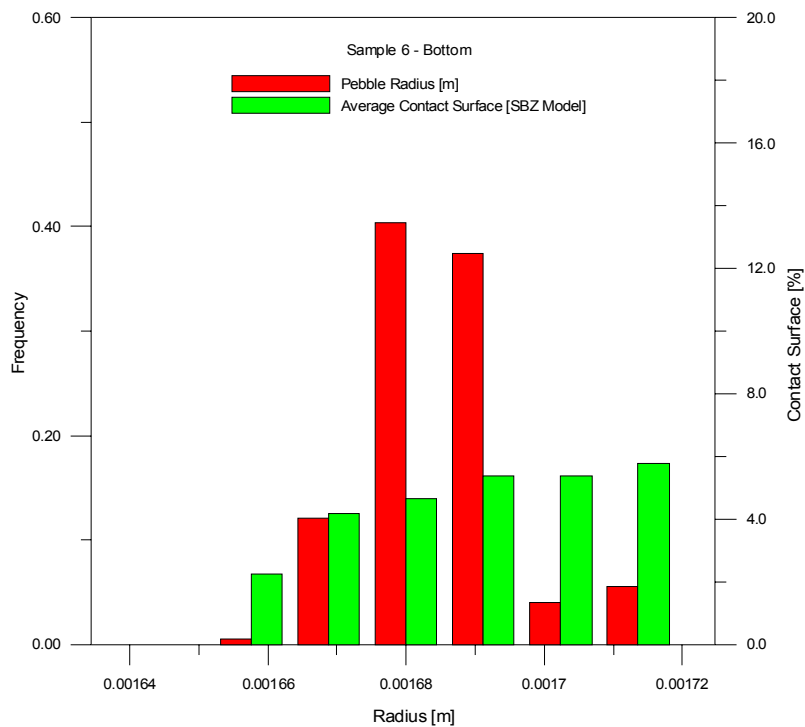


Fig. A.13 – SBZ model contact index by pebble radius size distribution frequency (in green) for sample 6 - bottom

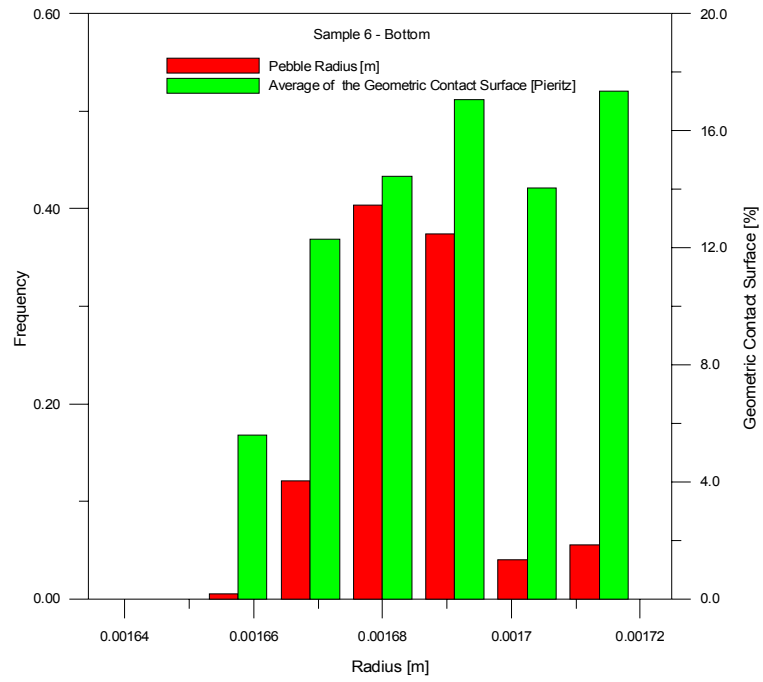


Fig. A.14 – Geometric contact surface index (as defined in section 4.4)) by pebble radius size distribution frequency for sample 6 – bottom.